Instrumentation and calibration protocol for imaging dynamic features in dense-scattering media by optical tomography

Christoph H. Schmitz, Harry L. Graber, Hengbin Luo, Imran Arif, Jai Hira, Yaling Pei, Avraham Bluestone, Sheng Zhong, Randy Andronica, Ira Soller, Nestor Ramirez, San-Lian S. Barbour, and Randall L. Barbour

Instrumentation is described that is suitable for acquiring multisource, multidetector, time-series optical data at high sampling rates (up to 150 Hz) from tissues having arbitrary geometries. The design rationale, calibration protocol, and measured performance features are given for both a currently used, CCD-camera-based instrument and a new silicon-photodiode-based system under construction. Also shown are representative images that we reconstructed from data acquired in laboratory studies using the described CCD-based instrument. © 2000 Optical Society of America

OCIS codes: 170.3880, 170.3890, 170.1610, 170.5380, 170.3830.

1. Introduction

The field of optical tomography has advanced to the state in which several groups are currently developing instrumentation for clinical studies.[1–10] Efforts to optimize data collection and analysis strategies invariably require the weighing of trade-offs between instrument complexity, computational burden, and the quality and reliability of information that is derivable from the resultant images. As is evident from the large number of reports in the literature describing various approaches to data collection (e.g., illumination conditions,[11,12] source–detector number, and geometry[13,14]) and analysis (e.g., choice of physical model,[15] numerical methods, and reconstruction algorithm[16]), there is a large parameter space within which to consider these trade-offs.

Implicit in most of these is the expectation that the dominant contrast features that exist naturally in tissue do not vary appreciably within the time frame of measurement. Although this is a reasonable premise with respect to features that are detectable by other imaging modalities (e.g., the soft tissue contrast that is detectable by magnetic resonance imaging is essentially time invariant[17]), it is unlikely to hold for optical measurements, given their sensitivity to hemoglobin (Hb) levels and its oxygenation state. This is an important distinction because, although it seems likely that functional information other than that linked to variations in Hb states also will be discernible from optical examination of tissue,[18–20] it is clear that noninvasive studies of Hb states are one of its most important prospective applications.

Two issues influencing the approach taken by investigators in optical tomography are the known reactivity of the vasculature and the fact that the external boundary of tissue is basically irregular. A hallmark of the vascular system is the speed and magnitude with which abrupt changes in the local perfusion state of tissue can occur.[21] Provocation by exercise,[22] temperature,[23] or vasoactive agents[24] can produce changes in flow of the order of several hundred percent within a few seconds or less. Moreover,

C. H. Schmitz, H. L. Graber, A. Bluestone, R. Andronica, I. Soller, and R. L. Barbour (rbarbour@netmail.hscbklyn.edu) are with Downstate Medical Center, State University of New York, Box 25, 450 Clarkson Avenue, Brooklyn, New York 11203. C. H. Schmitz, H. L. Graber, A. Bluestone, and R. H. Barbour are with the Department of Pathology. R. Andronica and I. Soller are with the Scientific and Medical Instrumentation Center. H. Luo, S. Zhong, and R. L. Barbour are with the Polytechnic University, 6 Metrotech Center, Brooklyn, New York 11201. H. Luo is with the Department of Computer Science. S. Zhong and R. L. Barbour are with the Department of Electrical Engineering. When this research was performed, I. Arif was a student at Midwood High School, 2839 Bedford Avenue, Brooklyn, New York 11210, and J. Hira was a student at North Shore High School, 450 Glen Cove Avenue, Glen Head, New York 11545. Y. Pei, N. Ramirez, and S.-L. S. Barbour are with NIRx Medical Technologies Corporation, 15 Cherry Lane, Glen Head, New York 11545.

Received 8 June 2000.
0003-6935/00/346466-21$15.00/0

a variety of methods have demonstrated that microvascular perfusion of tissue exhibits significant spatial and temporal variations even at rest.[25,26] In addition, it is well appreciated that there is insufficient blood in the body to simultaneously perfuse the entire vascular bed.[27] Instead, the vasculature is continuously shunting blood first through one region of tissue and then another. This process is modulated primarily by autonomic activity and is further modulated by local metabolic needs.[28]

To obtain optimal image quality, it is important to match data collection strategies with the expected influence of vascular reactivity. For example, knowledge that the temporal point-spread function of light is measurable in tissue has motivated some to employ time-resolved detection methods combined with ultrafast laser sources.[29,30] Although it is the case that the greatest spatial information is contained in a time-resolved signal, tomographic measurements made with this technology require data-acquisition times on a time frame of minutes to derive data having acceptably low noise levels.[5] The difficulty with this approach is that it conflicts with the expected influence of vascular reactivity. Variations in the latter will tend to effectively homogenize the background contrast. It follows that measurements that employ signal-averaging techniques may well have lower contrast and resolution than could be derived from a rapid measurement. It is important to recognize that this is not a consequence of any limitation originating from the physics of photon transport in tissue, nor to any that may exist with a particular reconstruction algorithm. Instead, it is because the dominant contrast features measurable at near-infrared wavelengths in tissue are themselves intrinsically dynamic. In this regard, it can also be expected that the information derived from any discrete measurement will have a higher variance than would exist if the feature of interest were intrinsically static. The second issue important to data collection is the complications that may arise from contact-based measurements performed on targets having irregular geometries. It is useful to recognize that this issue is not encountered in most nonoptical tomographic imaging modalities used in clinical investigations. The apparent need for direct contact between optical fibers and the skin (or other surface) when optical measurements are performed raises concerns regarding the fidelity of contact, as this can influence the coupling efficiency of light delivered to and exiting from the tissue. Variability of this type can be expected to distort the information that is retrievable from image maps, because most model-based image reconstruction schemes implicitly assume equivalency between computed and measured detector responses.

Another requirement frequently imposed by these methods is the assumption of accurate knowledge of the external geometry of the target medium. Although such concerns can be partially mitigated by immersion of the target into an index-matching scattering medium, thereby effectively extending its boundary, this approach seems impractical for most applications being considered (e.g., monitoring in acute care situations, brain imaging). Still another concern is the observation that tissue structures exist in a wide range of shapes and sizes. This holds importance because of the further implicit assumption by the imaging algorithms that the position of each measuring probe is known relative to all others. This information is not readily had by simply placing a measuring device on the surface of a target that has an arbitrary geometry. Thus it would seem that conditions for optimal data collection would include the need to perform time-varying, contact-based measurements and an accurate knowledge of the location of all measuring probes on tissue structures that have varying sizes and external geometries.

In this paper we describe our efforts to develop instrumentation that is capable of meeting these requirements. Critical design features include the ability to perform time-varying, parallel, multiwavelength measurements over a broad dynamic range (up to $\sim 10^9$) and use of geometrically adaptive measurement heads that are suitable for the investigation of varying tissue structures. A description of the current instrumentation, its design rationale, and representative imaging results from laboratory studies, as well as that of a model-independent calibration scheme, is presented. Also presented are the rationale and measured performance features of a new imaging system under construction, which is capable of acquiring parallel multisite, multiwavelength measurements at sampling rates of up to 150 Hz. These systems can achieve detection sensitivities of under 1 pW (CCD camera) or ~10 pW [photodiodes (PD's)] noise-equivalent power (rms), with signal averaging times of the order of 1 ms. For a source power of, say, 40 mW directed to tissue having properties of $\mu_a = 0.1\ \mathrm{cm}^{-1}$ and $\mu_s' = 10\ \mathrm{cm}^{-1}$, signal levels at least ten times in excess of these noise floors would be obtained for full transmission measurements of structures up to at least 10 cm in thickness.

2. Design of a CCD-Camera-Based Fast Optical Tomographic Imager

The system functionality, described previously in preliminary form,[4] of the CCD-based system is based on an alternating-source, parallel-detection scheme. Figure 1 shows a block diagram of the instrument currently being used and illustrates four functional units: (1) light source with power supply and demultiplexer; (2) one of several available measuring heads; (3) parallel attenuator and CCD array; and (4) controller. Each is described in more detail below.

A. System Components

1. *Source and Illumination Scheme*

Light Source. Target illumination is achieved by use of two temperature-regulated laser diodes (785 and 810 nm) that are operated at constant intensity. Each laser diode has an attached pigtail fiber that is

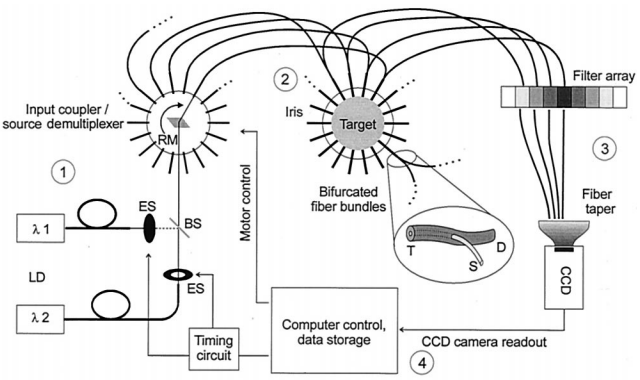

Fig. 1. Block diagram of the existing CCD-based instrument. LD, laser diodes at two different wavelengths λ1, λ2; ES, electronic shutter; RM, rotating mirror; T, target facing end of fiber bundle; S, source fiber; D, detector fiber; BS, beam splitter. Numbers indicate different functional features of instrument described in text.

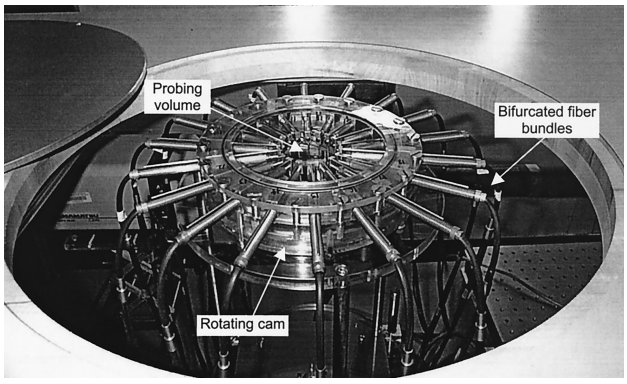

Fig. 2. Photograph of the iris measurement head.

ended with a gradient-index-rod lens to form a collimated beam. The two beams are combined into a single axis by use of a beam splitter. Positioned between the fiber end and the beam splitter are electronic shutters, operated under computer control, that serve to alternately direct light from one source and then another into the optical multiplexer. The lasers that are used are capable of producing light intensities of the order of 400 mW. Of this, however, only ~30% is available for target illumination because of coupling losses with the optical fibers. Typically we find that only 5–10 mW of optical power is needed for studies on the human forearm.

Optical Demultiplexer. This unit houses the electronic shutters, coupling optics, and stepper motor required for automated control of target illumination. These units serve, respectively, to optically chop light in an alternating fashion, colinearize the two beams along a single axis, deflect the light into the plane of the transmitting fibers, and sequentially reposition the source beam into the fiber optics that are arranged in a uniform circular array lying in a plane orthogonal to the incident beam axis. The source-fiber array is composed of 18 1-mm-diameter fiber-optic bundles positioned at 20° intervals. These terminate at the imaging head(s) described below, where they are surrounded by a halo of collecting fibers forming a bulls-eye configuration.

2. *Imaging Heads*

A key functional component of the imaging system is the imaging head, for which three different designs were constructed, each for use in a different set of intended applications. All have the feature of being geometrically adaptive in some manner.

Iris. The device most extensively studied thus far is shown in Fig. 2. This unit is intended for examination of structures, such as limbs, that readily can be made to adopt a cylindrical shape. It basically consists of a mechanical iris to which are attached optical fibers that deliver light to, and collect light emerging from, a target. The iris unit houses 18 fiber bundles positioned uniformly about a circle at 20° intervals. Space for an additional 18 fiber bundles is available. The pass-through diameter of the iris is continuously adjustable over a range of 3–13 cm. This is achieved mechanically when the position of the cam device that actuates the iris opening is adjusted in a rotary fashion. Two handles, located at the ends of a diameter, are attached to the cam device for operator control. The iris itself is composed of 18 curved blades that form a circle at all pass-through diameters. The optical fibers are attached to the blades in a spring-loaded fashion. Each fiber bundle is housed in a brass tubing that passes through a metal block positioned near the opening of the iris. The back end of the tubing is spring loaded against this block. This ensures that the fiber bundles retain the circular geometry imposed by the iris at all diameters. The optical fibers contained in the iris are bifurcated at the target end. The receiving bundle is 3 mm in diameter and terminates at the variable attenuator. The length of each arm of the bundle is 8 ft (2.44 m). Although adjustable, the iris unit is quite rigid. This serves to mechanically stabilize a target under examination (e.g., a forearm) against motion artifacts, while gently conforming its external geometry to a circle.

Pad. Figure 3 shows photographs of the imaging pad. This device was constructed for investigations of structures that are too thick to allow transmission measurements, and it consists of 18 bifurcated transmitting and receiving fiber bundles and 45 receiving-only bundles, arranged in a 7×9 array. The unit is flexible in both dimensions and can be held in contact with tissue by means of an adjustable belt (not shown) to collect backreflected light. The optical fiber bundles are held in place by a serrated black rubber belt of the sort commonly used in automobiles, through which holes to contain the optical fibers were drilled. We achieved significantly increased flexibility by removing rubber between each pair of adjacent links. The set of seven strips, each holding nine fibers, is held together as a unit by attachment to a

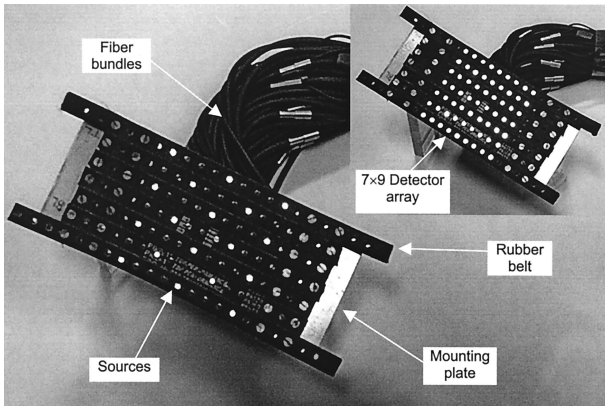

Fig. 3. Photograph of the pad measurement head showing the arrangement of the source fibers. Inset: The array of 9 × 7 detector fibers.

metal plate on each end. Although any arrangement of fiber geometries can be adopted, the one chosen (see Fig. 17) would appear optimal for backscatter investigations (see Section 5).

Folding Hemisphere. Figure 4 shows a picture of the imaging head used for investigations of the breast. This device is based on a folding geometry in the form of one half of a trapezoidal icosatetrahedron. Similar to the iris design, the unit retains a fixed geometry (i.e., a hemisphere) at all diameters. This configuration is based on a design previously described by Hoberman[31] and originally intended for nonmedical applications. The unit consists of a folding iris to which additional out-of-plane folding structures that form eight evenly spaced hemispheric arcs

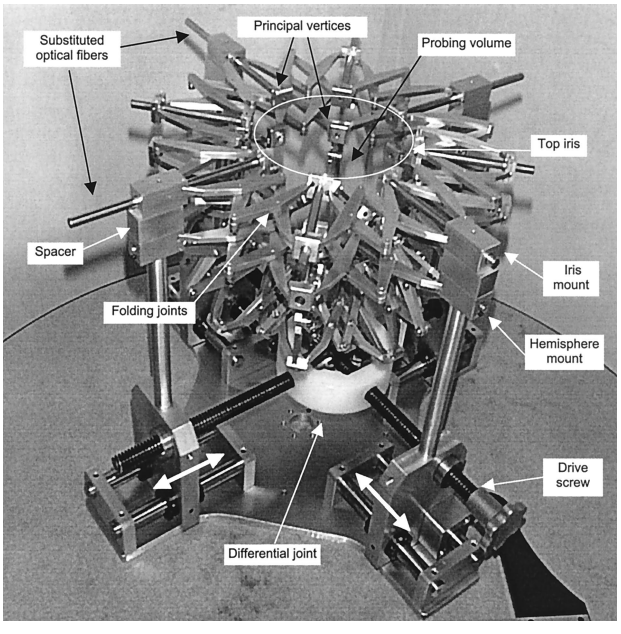

Fig. 4. Photograph of a folding hemisphere structure, consisting of a folding hemitrapezoidal icosatethrahedron. Top-most device is an additional folding iris. Various functional features described in the text are identified.

are attached. In the imaging head shown in Fig. 4, the basic design was extended to accommodate one additional folding iris whose diameter and height above the hemisphere are independently adjustable.

The basic hemisphere contains 17 principal vertices, through each of which a fiber bundle is allowed to pass (labeled Substituted optical fibers in Fig. 4). As shown, the unit has 25 principal vertices because of the presence of one additional folding iris mounted on top of the hemisphere. Additional fiber bundles can be introduced into the folding structure by attachment to the 12 minor vertices associated with the out-of-plane folding structures. If required, still more fiber bundles can be introduced between the folding structures and within the plane of each folding iris. We can adjust the diameter of the folding hemisphere and the additional attached irises by turning a lead screw that actuates a differential joint, thereby effecting uniform extension or contraction of the unit along the two principal axes. This device is intended mainly for investigations of a breast suspended in a pendant position.

It is our experience that, primarily as a function of size, a given breast will naturally tend to assume one of two basic geometries when the folding structure is closed to come into gentle contact with the tissue. Smaller breasts can readily assume a hemispheric geometry without causing discomfort. Larger breasts assume more of a teardrop shape in the pendant position and cannot be made to conform to a hemispheric geometry and still have the device positioned close to the chest wall without causing undue discomfort. For this reason we incorporated an additional folding iris (more than one can be added) into the measurement head design to permit contact measurements near the chest wall. With this, we observed that gentle, high-fidelity contact measurements could be made simultaneously at all measuring points. The diameter of the hemisphere is continuously adjustable over a range of 5–20 cm.

3. *Signal Conditioning and Detection*

Variable Attenuator. This unit serves to extend the dynamic range of the CCD camera, which is nominally limited to 14 bits. An extended measuring range is needed, because the anticipated dynamic range required for measurements that include both backreflection and transmission measurements (i.e., full tomographic) is typically of the order of 7–9 decades (i.e., 24–30 bits), depending on tissue size. We considered three different designs, one for each measuring head. The unit most extensively tested is shown in Fig. 5 and is intended for use with the iris measuring head. The motivation for its design is the recognition that, for structures having nearly cylindrical geometry (i.e., a limb), the dynamic range of measurement is, within an order of magnitude, nearly independent of the source position and approximately bilaterally symmetric.

The unit shown in Fig. 5 consists of a nested cylinder housing two sets of fibers that are positioned

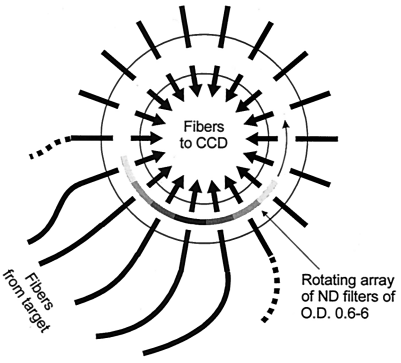

Fig. 5. Detailed schematic of the variable attenuator array. O.D., optical density.

such that one end of each fiber in the first set is opposed by a second across a narrow groove that houses the attenuator array. One set of fibers conducts light to the unit from the imaging head while the other collects light passing through the attenuator and then directs it to the fiber taper mounted to the CCD camera. Both sets consist of 18 fiber bundles, each 3 mm in diameter, terminated by custom-made 6-mm-diameter metal sleeves. Positioned between the fiber bundles is a thin (1-mm-thick) rotatable cylinder to which neutral- density (ND) Wratten filters having varying attenuation values are attached. The latter are fixed to 6-mm-wide shallow channels [0.015 in. (0.04 cm) deep] that contain a 3.5-mm-diameter pass-through hole. The greatest attenuation (of the order of 10^6) is limited to light collected by the detector fibers that are coaxial with the source fiber (i.e., the detector is collocated with the source). This value falls gradually to zero for fibers positioned at greater distances from the source. To maximize the light collection efficiency, the distance separating the opposing bundles in the attenuator assembly is <1.2 mm. To maintain appropriate attenuation levels for all detector fibers, we synchronize the manual rotations of the filter array with our repositioning of the illuminating source fiber.

The attenuator unit used with the imaging pad (not shown) has a functionality similar to that used with the iris but was modified to accommodate one additional spatial dimension of measurement. In this case we employ a thin ($<$1-mm-thick) two-dimensional (2-D) array having the appearance of a bulls-eye target fitted to a square mesh. The attenuation is greatest at the center and decreases with increasing radial distance until no further attenuation is needed to operate within the dynamic range of the camera. The attenuation array itself is positioned between a mount housing the fibers that collect light from the pad and the front face of the fiber-taper–CCD assembly. To improve coupling efficiency, the distance separating the mount and the taper is <1.5 mm. The surface area of the fiber taper is sufficiently large to measure all 63 detecting fibers housed within the pad in parallel. This unit, together with the 2-D attenuator, was tested on the leg, neck, and torso of an adult and proved capable of providing good-quality data across the entire array (signal-to-noise ratio levels $>$10:1) for detector fibers at distances up to 9 cm from the source at a 4-Hz measuring rate.

Measurements involving the hemisphere include a third spatial dimension and hence require an appropriate design modification to the attenuator array to achieve full tomographic views. We achieved this using a design (not shown) that is a hybrid of those used with the pad and iris. In this case we use a 2-D attenuator array of the sort employed with the pad and mount this to a rotatable nested cylinder similar to that used with the iris. We also allow for vertical translation of the 2-D array to accommodate source positions in the hemisphere that are out of plane with respect to the top iris.

Detector Array. Our desire to achieve parallel measurement for multiple fiber positions imposes the need for efficient coupling of light from the detecting fibers to the CCD array. A simple and economical solution is to mount a fiber taper to the CCD array, thereby effectively increasing its collecting area. We recognize that fiber-to-fiber coupling typically is inefficient; however, this is more than offset by the lensing effect introduced by the fiber taper. The taper we use has a 4:1 front-to-back diameter ratio and hence can potentially enhance light intensity presented to the CCD array by a factor of 16. The taper actually employed was cut so that its front face is a 7 cm $\times$ 7 cm square. For each measuring head, we designed mounting plates that rigidly hold the fiber ends and that can be placed in contact with the front face of the taper, thereby enhancing the coupling of light to the CCD array. The image formed on the array amounts to a series of spots, one for each fiber bundle. The number of spots seen is a function of which imaging head is used. For the fibers we used, the surface area of the fiber taper is capable of accommodating a maximum of 81 fiber bundles while retaining sufficient interfiber space for the mounting hardware. The acquisition speed is currently limited by the read time of the CCD camera. When short exposure times ($<$50 ms) are used, image capture rates are restricted to $\sim$4 Hz for studies involving a single wavelength of light, or to $\sim$2 Hz for dual-wavelength measurements.

4. Controller

Instrument Software. Motion control software, obtained from the manufacturer of the motor (Parker Hannifin Corp.), was used to actuate repositioning of the optical demultiplexer. This can be performed discretely or in a preset time series (e.g., 20° start–stop–dwell movements). Controlling software for the CCD camera was provided by MedOptics and was customized for time-series measurements. User-selectable features include the binning size, acquisition time, and number of images captured within a given time-series measurement. For example, in the experimental studies performed so far, we typi-

cally used 6 × 6 binning, 10-ms integration times, and collected as many as 1440 consecutive images. The upper limit is determined by the amount of available RAM, which for the computer system used (Dell Dimension XPS R400) was 128 Mbytes. Collected image data were transferred to disk and subsequently analyzed by our determining the average intensity seen in each spot corresponding to light emerging from a receiving fiber. We accomplished this by using a simple thresholding scheme to determine the boundary of each spot. The derived values were corrected for dark current and, when necessary, for the varying coupling efficiencies of the transmitting and receiving optics.

Shutter Timing Circuitry. Normal operation of the MedOptics camera requires use of an electronic shutter to avoid streak artifacts that are due to signal accumulation during the read time. On exposing the CCD array, the supply–control unit used with the camera delivers a transistor-transistor logic- (TTL-) compatible signal that can be used to trigger external devices. Because we need to alternately activate two shutters—one for each wavelength—we developed a small digital circuit functioning as a toggle flip-flop. This serves to send actuating pulses to the shutters in an alternating fashion. Inhibiting this mechanism, and driving only one of the two shutters, we achieve single-wavelength operation.

B. Materials

Commercially available components used in the instrument design include the following. The laser power supply (Model 8000), equipped with Model 8630 laser diode driver and thermoelectric cooler controllers, was obtained from Newport Corp., Irvine, Calif. Pigtail laser diodes (Model HPD101-BUTF-TEC), operating at 780 and 810 nm, were purchased from High Power Devices, New Brunswick, N.J. The output light is collimated (divergence angle $<2°$) by use of a gradient-index-rod lens, and the maximum operating output power is 400 mW. The electronic shutters and controllers (Models 04IES001 and 04IES004, respectively) were purchased from Melles-Griot, Rochester, N.Y. Fiber bundles consisting of 50-μm-diameter cladded glass fibers, 8 ft. (2.44 m) in length, were obtained from Fiber Optic Systems, Inc., Simi Valley, Calif. We perform motion control of the optical demultiplexer by use of a Model Zeta57-51 stepper motor powered by a Zeta6104 index driver, both obtained from Parker Hannifin Corp., Rohnert Park, Calif. Optical detection is performed with a 14-bit Model K1000-CAL cooled CCD camera obtained from MedOptics Corp., Tucson, Ariz. A 7 cm × 7 cm fiber taper was mounted to the array. The folding hemisphere was obtained from NIRx Medical Technologies Corp., Glen Head, N.Y. All other devices were fabricated in-house by the Scientific and Medical Instrumentation Center, Downstate Medical Center, State University of New York. Computer-controlled devices include the electronic shutters, the optical multiplexer, and the CCD camera.

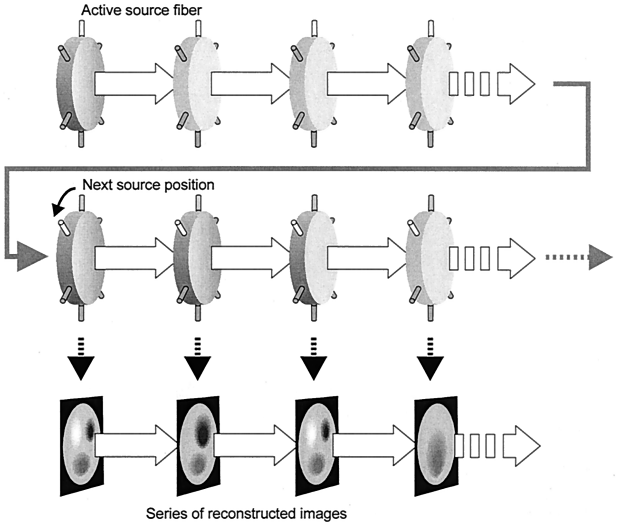

Fig. 6. Timing scheme for dynamic measurements performed with the existing setup.

C. Data Capture Scheme

Time-series measurements can be performed according to either of two schemes. Figure 6 shows the arrangement typically pursued with the current instrument design. This shows a serial measurement being performed for each source location. Parallel data collection speeds of up to 4 Hz are available, 2 Hz if two sources are used. This rate is limited by the read time of the CCD camera and not by the required acquisition time, which is typically <10 ms for most investigations. The total measurement time is equal to the time for each serial measurement multiplied by the number of source locations. This approach makes the assumption that the temporal variations that occur within the target can be reproduced for every source in succession. For phantom studies, this is easily accomplished. For physiological studies, this can be approximated when some form of provocation is introduced, followed by sufficient recovery time.

An alternative approach is to perform a single time-point parallel measurement at each source position and switch between source positions at a rate that is fast compared to the highest large-amplitude temporal frequency present in the target. With the CCD-based system, switching rates of $\sim 1/s$ are possible when the source demultiplexer is mechanically linked to the variable attenuator, causing them to move synchronously. In practice, however, the mechanical load of the attenuator renders this approach nonreproducible because of the load it places on the motor being used. Although this limitation could be overcome with a more powerful motor, it is unlikely to work at the speeds attainable when electronic switching designs are used, which is the approach taken in

the silicon-photodiode- (SiPD-) based device described in Section 3.

D. Multichannel Calibration Scheme

In this section we describe methods for system calibration that are applicable to all the measuring heads described. Our goal in performing such measures is to account for losses unrelated to those caused by the target medium so as to allow for more quantitative comparisons of the computed image data. Motivating our considerations has been an appreciation of the practical constraints imposed by clinical environments. Thus we sought to devise schemes that not only account for varying systematic performance among the measuring channels but that also provide statistical measures that facilitate system troubleshooting in the case of component (system) degradation or failure. Although it is likely that a variety of approaches to calibration could be adopted, not all are equally capable of addressing these constraints. For example, the sensitivity of an optical fiber's transmission efficiency to bending or torsion suggests that system calibration should proceed with the instrument fully assembled and all components disposed as they would be during an actual measurement. In addition, systems of the type described are prone to degraded performance as a result of contamination of optical surfaces. Detection of this and identification of the involved component(s) has practical value. The approaches that are described next meet both of these criteria.

In the following mathematical treatment, we make several explicit assumptions. These include the following: (i) neither the target medium nor the optical detector exhibit nonlinear behavior with respect to the optical power propagating through the target and measuring system; (ii) all source intensities and detector efficiencies are time invariant; and (iii) each detector reading is a measure of light that has entered a target medium at only a single location (i.e., one illuminating source fiber), and that the light which is detected has exited from only a single location.

It is convenient to divide the calibration problem into three components, i.e., factors associated with the source fiber, with the target medium, and with the detecting fiber. Equation (1) is a simplified parametric description of the loss terms that account for the fraction of light produced by a source that ultimately enters the target:

$$I_{s,i} = \alpha_{s,i}\beta_{s,i}\gamma_{s,i}P_l \equiv s_i P_l. \tag{1}$$

Here P_l is the laser power and $I_{s,i}$ is the fraction of light entering the target at the ith source fiber position. The terms $\alpha_{s,i}$, $\beta_{s,i}$, and $\gamma_{s,i}$ account for the attenuation along the optical path resulting from imperfections when laser light is coupled into the source fiber (e.g., from misalignment or from optical surface reflections), transmission losses in the fiber (primarily a consequence of bending), and the fraction of light that enters the target (e.g., from reflection of a fraction of the light off the surface the target), respectively. The quantity s_i can be taken as the overall source coupling efficiency coefficient, whose value will vary for each optical path.

Similarly, Eq. (2) is a simplified parametric description of the loss terms that account for the fraction of light that exits the tissue at receiving fiber position j and ultimately enters the detector:

$$I_{d,j} = \alpha_{d,j}\beta_{d,j}\gamma_{d,j}\delta_j I_{t,j} \equiv d_j I_{t,j}. \tag{2}$$

Here $I_{t,j}$ is the fraction of light exiting the target at the jth receiving fiber position and $I_{d,j}$ is the fraction that ultimately reaches the detector. The loss terms $\alpha_{d,j}$, $\beta_{d,j}$, $\gamma_{d,j}$, and δ_j correspond to coupling losses at the target–receiving fiber interface, fiber transmission losses, coupling loss at the receiving fiber–detector interface, and additional losses introduced by the variable attenuator array, respectively. The quantity d_j is the corresponding composite loss term for the detecting fibers. Its value also will vary for each optical path.

The influence of the target medium on light propagation through the system is described by the quantity m_{ij}, which is the fraction of photons launched into the target at location i that, traveling through the medium, exits at location j. Using Eq. (1), we can express this as $I_{t,ij} = m_{ij}I_{s,i} = s_i m_{ij} I_l$, where $I_{t,ij}$ is the amount of light exiting the target at detector position j, originating from source position i. Finally, by introducing the composite loss term from Eq. (2), we can model the transfer function of the entire measurement scheme as $T_{ij} = s_i m_{ij} d_j P_l$, where the $i \times j$ values of T_{ij} represent the power read by the detector acquired from the jth detector position with respect to the ith source position. In an experiment, the $i \times j$ detector readings are described by the expression $r_{ij} = cI_{ij}$, where c is the detector sensitivity, assumed to be constant across the CCD array. Using these last two relations, we can formulate our model for the transfer function as a matrix equation

$$\mathbf{R} = cP_l\mathbf{SMD}, \tag{3}$$

where the elements in $\mathbf{R}$ are the detector readings r_{ij}; $\mathbf{S}$ and $\mathbf{D}$ are diagonal matrices whose elements represent the composite loss factors d_j and s_i, respectively; and the elements in matrix $\mathbf{M}$ are the m_{ij} values attributable to losses occurring in the medium. The goal of calibration is to determine the entries of $\mathbf{D}$ and $\mathbf{S}$, given the set of measured values in $\mathbf{R}$. We recognize, however, that there is no unique factorization of $\mathbf{R}$ in Eq. (3) to yield the desired coefficients. For example, if the ith(jth) diagonal element of $\mathbf{S}$($\mathbf{D}$) is multiplied by an arbitrary constant $u_i(v_j)$ (u_i, $v_j \neq 0$), and the ith(jth) row(column) of $\mathbf{M}$ is multiplied by $u_i^{-1}(v_j^{-1})$, then the product $\mathbf{SMD}$ is unchanged. Therefore we must use information about $\mathbf{M}$ that leads to some type of expected response, such as would arise, for example, as a result of imposed symmetry.

In the case of the iris measuring head, our start-

ing point is a dense-scattering phantom that has a circular shape in the plane of measurement and is structurally homogeneous. (Strictly, for this measurement geometry the medium need be homogeneous in the angular dimension only, but may possess any degree of heterogeneity in the radial dimension.) Simple symmetry considerations lead then to the following form for our matrix equation:

$$\begin{bmatrix} r_{11} & r_{12} & \cdots & r_{1N} \\ r_{21} & r_{22} & \cdots & r_{2N} \\ \vdots & \vdots & \ddots & \vdots \\ r_{N1} & r_{N2} & \cdots & r_{NN} \end{bmatrix} = \begin{bmatrix} s_1 & 0 & & 0 \\ 0 & s_2 & \ddots & \\ & \ddots & \ddots & 0 \\ 0 & & 0 & s_N \end{bmatrix} \times \begin{bmatrix} m_1 & m_2 & & m_N \\ m_N & m_1 & \ddots & \\ & \ddots & \ddots & m_2 \\ m_2 & & m_N & m_1 \end{bmatrix} \begin{bmatrix} d_1 & 0 & & 0 \\ 0 & d_2 & \ddots & \\ & \ddots & \ddots & 0 \\ 0 & & 0 & d_N \end{bmatrix}, \quad (4)$$

where **M** now is of the form of a constant-diagonal (Toeplitz) matrix. We wish to point out that our approach makes no further assumptions about the light propagation inside the test object and that no particular physical model of photon propagation is applied to the problem. Even with this added constraint there are still infinitely many ways to factor **R** into the form indicated by the right-hand side of Eq. (4); just as for Eq. (3), when $s_i(d_j)$ is multiplied by any nonzero $u_i(v_j)$ and the ith(jth) row(column) of **M** is multiplied by ${u_i}^{-1}({v_j}^{-1})$, the product **SMD** is preserved. However, only those modifications that preserve the relative values of all the d_j and all the s_i will also preserve the constant-diagonal structure of **M**. It follows that any particular factorization that has the form given by the right-hand side of Eq. (4) can be expected to contain an accurate determination of the relative values for d_j and s_i, which we refer to as the relative coupling efficiencies. It is for this reason as well that we no longer show the quantities c and P_l that determine the absolute value of readings r_{ij} in Eq. (4).

We developed two algorithms for determining the relative coupling efficiencies associated with the system transfer function for our measuring system. The first method enforces a constant-diagonal structure on **M**, whereas the second method does not constrain **M** in any particular way. If the three-factor model of Eq. (4) is not appropriate for a given **R**, this will be revealed by the various estimates of each s_i and d_j being grossly unequal when the first algorithm is used and by the production of an **M** that is not even approximately constant diagonal when the second algorithm is used. Also, whichever method is used, the product **SMD** will not closely approximate **R** in situations where any of the assumptions stated above are violated. As discussed below, this has the desirable feature of identifying potential problems originating from system degradation.

The first method uses Eq. (4) and then makes the further assumption that **M** is symmetric. Hence, because of the object's structure and geometry, under ideal conditions the detector reading measured at an angle $+x°$ and $-x°$ from the point where light is incident should be exactly be the same. For the case of 18 sources and 18 detectors per source, as found in the iris, **M** has the form

$$\mathbf{M} = \begin{bmatrix} m_1 & m_2 & \cdots & m_9 & m_{10} & m_9 & \cdots & m_3 & m_2 \\ m_2 & m_1 & \ddots & & \ddots & \ddots & \ddots & & m_3 \\ \vdots & \ddots & \ddots & \ddots & & \ddots & \ddots & \ddots & \vdots \\ m_9 & & \ddots & \ddots & \ddots & & \ddots & \ddots & m_9 \\ m_{10} & \ddots & & \ddots & \ddots & \ddots & & \ddots & m_{10} \\ m_9 & \ddots & \ddots & & \ddots & \ddots & \ddots & & m_9 \\ \vdots & \ddots & \ddots & \ddots & & \ddots & \ddots & \ddots & \vdots \\ m_3 & & \ddots & \ddots & \ddots & & \ddots & m_1 & m_2 \\ m_2 & m_3 & \cdots & m_9 & m_{10} & m_9 & \cdots & m_2 & m_1 \end{bmatrix}. \quad (5)$$

Applying Eq. (4), we find that this special form of **M** yields multiple representations of the ratios of the main diagonal element to all eight other entries (i.e., $m_1/m_2, m_1/m_3, \ldots$) when we appropriately combine four matrix elements of **R**. For example,

$$\left(\frac{r_{1,1}r_{2,2}}{r_{1,2}r_{2,1}}\right)^{1/2} = \left[\frac{(s_1m_1d_1)(s_2m_1d_2)}{(s_1m_2d_2)(s_2m_2d_1)}\right]^{1/2} = \frac{m_1}{m_2} = \left(\frac{r_{2,2}r_{3,3}}{r_{2,3}r_{3,2}}\right)^{1/2} = \left(\frac{r_{3,3}r_{4,4}}{r_{3,4}r_{4,3}}\right)^{1/2} = \ldots. \quad (6)$$

Analogous expressions can be found for the ratios m_1/m_3, m_1/m_4, and so forth.

After having obtained the measured values that form **R**, we treat all values obtained for each m_1/m_j ratio with a robust outlier identification procedure[32] to decide whether they are sufficiently close to conclude that they are estimates of a single quantity.

With this knowledge, we can also determine the diagonal (i.e., nonzero) elements of the matrices **S** and **D**. Note that, for example,

$$\frac{r_{1,1}}{r_{2,1}} = \frac{s_1m_1d_1}{s_2m_2d_1} = \frac{m_1}{m_2}\frac{s_1}{s_2}, \quad \frac{r_{1,1}}{r_{1,2}} = \frac{s_1m_1d_1}{s_1m_2d_2} = \frac{m_1}{m_2}\frac{d_1}{d_2}, \quad (7)$$

and by substituting in the mean value of m_1/m_2 obtained in the previous step, we can obtain multiple estimates of s_1/s_2 and d_1/d_2. Many other pairs of elements of **R** can likewise be combined to give multiple estimates of the ratios of other elements of **S** and **D**.

The second procedure we developed does not assume *a priori* that **M** is symmetric. The idea is to take an experimentally measured **R** and to apply (although without a rigorous justification) the iterative proportional fitting (IPF) technique.[33] That is, to compute a sequence of matrices,

$$(\mathbf{R}')_{ij} = \frac{r_{ij}}{\sum_{j'=1}^{N} r_{ij'}}, \quad (\mathbf{R}'')_{ij} = \frac{r_{ij}'}{\sum_{i'=1}^{N} r_{i'j}'}, \ldots, \quad (8)$$

and continuing in this fashion until the sequence converges to some preselected criteria. This algorithm is most commonly employed in statistical anal-

yses of data that are organized into contingency tables (i.e., matrices). It is useful for revealing intervariable interactions that may be obscured by the existence of widely divergent row and column sums. Extended to our case, our hope was that we could use it to remove the effects of different incoupling and outcoupling efficiencies, thereby uncovering whatever underlying structure was present in the **M** matrix.

To determine whether the second approach has merit, we applied it to a synthesized **R** that was constructed by using a pseudorandom number-generating algorithm to assign numerical values to the nonzero elements of the matrices **D**, **S**, and **M**, with **M** being constant-diagonal and symmetric for testing purposes. After the IPF computations converged, the resulting matrix $\mathbf{R}^{(\infty)}$ was compared with the original **M**, element by element. We found that, within the limits of numerical error, $\mathbf{R}^{(\infty)}$ was equal to **M** times a scalar constant, thus validating the model.

When the IPF method was applied to sets of actual detector readings taken from homogeneous phantoms, the final answers were not perfectly symmetric or constant diagonal but were close on both accounts. Consequently, we averaged all the elements along each diagonal and used these averages to compute our estimates of m_1/m_n, $n = 2 - N$. These computations provided the data that are presented below in Section 4.

As the ultimate purpose of our performing this analysis was to produce estimates of the diagonal elements of **D** and **S**, after we had thus obtained estimates of the relative values of the elements of **M**, we divided each element of the original **R** by the corresponding element of the relative **M**; we call the resulting matrix **N**, where $n_{i,j} = ms_i d_j$ (m is the scalar constant alluded to above). Dividing each of **N** by its row sum, we obtain a number proportional to d_j:

$$n_{ij'} = \frac{ms_i d_j}{\sum_{j'} ms_i d_{j'}} = \frac{d_j}{\sum_{j'} d_{j'}} = m' d_j, \tag{9}$$

so every element in column j gives us an estimate of d_j. Likewise, dividing each element of **N** by its column sum, we obtain rows in which each element is an estimate of s_i. Just as for the first method, several independent estimates of each d_j and s_i are thereby produced, which allows us to compute various statistical measures.

E. Limitations of the CCD-Based Measuring System

Although the variable attenuator units described above are capable of significantly extending the dynamic range of the CCD camera, their mechanical design does not permit the fast repositioning that would be desirable for the above-indicated alternative approach to dynamic studies. Even if this could be accomplished with the current designs, to perform measurements on media of different sizes requires frequent changes of the ND filters, which is a tedious task. It would be better to introduce some form of electronics-based adaptive gain control or filtering that could be rapidly and synchronously adjusted in relation to fast source multiplexing.

Although we are aware that faster data capture rates are available with CCD formats, incorporation of a spatially variable adaptive gain control capability into a CCD array probably would be a daunting task. Our initial motivation for using a CCD array as the detector was the feasibility and ease with which parallel measurements could be acquired. It also has the advantage that the accumulation time is easily adjustable. However, even if we assume that the desired signal conditioning capability were available, use of a CCD format still retains two significant limitations. The first is the need to exclude ambient light. In principle, we could overcome this by modulating the source and incorporating a phase-locked detection scheme. Although we are unaware of this capability existing directly with a CCD array, we recognize that it could be effectively accomplished by modulating the gain to an image intensifier positioned between the detecting fibers and the CCD array.[34] However, although this possibility exists, it seems likely that use of such a device would interfere with described signal conditioning capability.

The second issue concerns the expected volume of data that could result from time-varying imaging studies when a CCD format is used. Even for modest studies, this could rapidly become burdensome. By comparison, the scheme outlined in Section 3 will produce data volumes of the order of 0.1%, or less, of that expected for CCD-based studies.

3. Fast Multichannel Silicon Photodiode Optical Imaging System

A. Performance Specifications

In this section we describe our SiPD-based instrument, whose design goals include improvement on the limitations indicated above for our current CCD-based instrument. The new instrument, which is still under construction, has undergone a period of preliminary testing, some results of which are presented here. We reiterate that all results on dynamic imaging and calibration studies discussed below were obtained from data collected with the CCD-based instrument.

A schematic of the new design introduced to overcome the restrictions of the CCD-based instrument is shown in Fig. 7. Because most of the limitations of the existing setup are imposed by the detection technology, our focus was principally directed to improving the performance features of this aspect of the instrument. The source switching modalities are basically the same as those of the CCD-based instrument, although we used a faster motor and introduced the capability of using as many as four wavelengths simultaneously. It is expected that the level of light power delivered to the tissue will not need to exceed 40 mW for many intended dynamic imaging studies of thick tissue structures (<10 cm in diameter.)

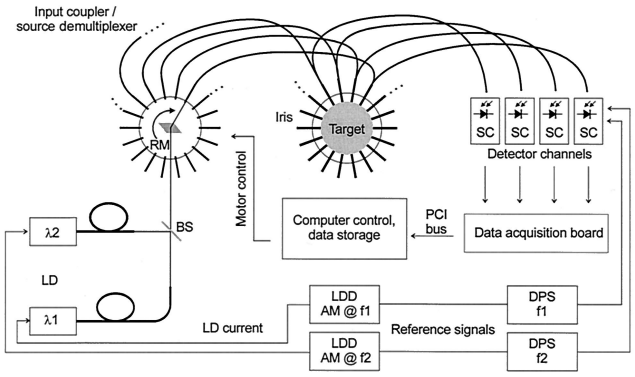

Fig. 7. Block diagram showing the principle of the new instrument design. LD, laser diodes; LDD, laser diode driver; AM, amplitude modulation; SC, signal conditioning circuitry (i.e., gain switch, lock-in, sample-and-hold circuit); DPS, digital phase shifter; RM, rotating mirror; BS, beam splitter; f1, f2, modulation frequencies; PCI, peripheral component interconnect.

Key to our design changes was the replacement of the CCD detector with an array of individual photodetector channels. System capability goals that guided these modifications were (1) large, linear dynamic measuring range (up to 10^9, 180 dB); (2) fast simultaneous detector readout rates (~150 Hz); (3) simultaneous, multiwavelength illumination; (4) fast source demultiplexing capability (~150 Hz); (5) insensitivity to ambient light; (6) use of geometrically adaptive measuring heads; and (7) system scalability and modular design.

To meet these requirements, we introduced three key design features that are illustrated for a single channel in Fig. 8: (1) use of digitally addressable measurement ranges to enhance the dynamic range of the system; (2) lock-in detection to reduce noise, reject ambient light, and permit simultaneous multiwavelength illumination; and (3) sample-and-hold (S/H) circuits to maximize detector sampling rates. The functionalities and the selection rationale for these are described Subsection 3.B.

B. Sensor Selection

The need to acquire signals whose levels cover a large dynamic range imposes particular requirements on the detector. Options here include several forms of semiconductor devices [photodiodes (PD's), avalanche PD's, p-i-n PD's], and photomultipliers. The latter are more light sensitive and can be used for single-photon counting, but they require a high-voltage supply (kilovolts) and do not provide sufficient dynamic range. Avalanche PD's have the highest light sensitivity among semiconductor devices (i.e., almost permitting single-photon counting), but they require a high reverse-bias voltage (~100 V) and exhibit strong temperature dependence. P-i-n PD's usually are operated with a reverse-bias voltage as well but at a much lower level (~10 V). This lowers their junction capacitance and increases their linear dynamic range but at the expense of increased dark current noise. These devices are most commonly used to detect high-frequency modulated signals, e.g., in telecommunications. An unbiased PD is the optimal choice of detector with respect to dark noise, cost, and ease of operation for the required frequency response and sensitivity of our application. They also show excellent linearity, over a wide range, between the incident radiation power and the produced photocurrent. We use a SiPD (Hamamatsu S1337 series) that has a relatively large sensitive area (5.8 mm^2) but a low junction capacitance (67 pF), which is desirable to reduce electric noise[35] generated in combination with the photoamplifier. The noise-equivalent power for the selected SiPD is 6.5×10^{-15} $W/Hz^{1/2}$.[36]

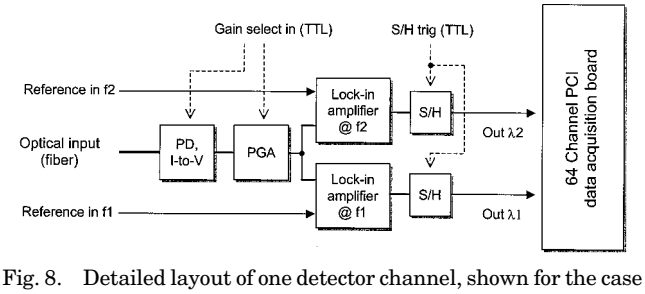

Fig. 8. Detailed layout of one detector channel, shown for the case of simultaneous measurements at two wavelengths. I-to-V, current-to-voltage converting amplifier; PGA, programmable gain amplifier; f1, f2, modulation frequencies; PCI, peripheral component interconnect.

C. Extension of Dynamic Range

To take advantage of the exceedingly large dynamic range of the type of SiPD used (>1:10^{10}), we operate it in the photoconductive mode, using a precision operational amplifier configured as a current-to-voltage converter (transimpedance amplifier) of low input impedance. Whereas this configuration delivers a voltage that varies linearly with the incident light power over a large dynamic range, the data-acquisition system itself is restricted to a certain—typically much smaller—signal range determined by its sensitivity, digital resolution, and saturation limit. We therefore seek to amplify our signal amplitude to a level between 1 mV and 10 V, to be well above the noise floor and to avoid saturation of the electronics. We address this task by electronically switching between two different feedback resistances at the transimpedance amplifier, thereby changing the photosensitivity by a factor of 10^3. We accomplish this using a miniature relay, which promises the best specifications with respect to leakage currents, parasite capacitances, and residual resistance, all of which constitute factors that can compromise the performance of the transimpedance amplifier. We favor this approach even though it is more power-consuming, slower, and shorter-lived than analog switches. The switching time (0.5 ms) is, however, still significantly fast compared with the settling time of the lock-in amplifier (see Subsection 3.D). Subsequent to this, a programmable gain amplifier with selectable gain factors (1× or 10^3×) is used, resulting in three mea-

surement ranges corresponding to three overall gain factors ($1\times$, $10^3\times$, $10^6\times$) by which the photosensitivity can be varied.

D. Lock-in Detection

Following the amplification, the signal is applied to a lock-in amplification stage. This approach is desirable for isolation of small signals against a larger noise background (e.g., such as that produced by ambient light). It is accomplished by use of a low-frequency signal (usually $<$20 kHz) both to modulate the source and to demodulate the amplified signal. By passing the demodulated signal through a low-pass filter (i.e., postdetection filter), we can exclude all noise components that are different from the modulation frequency. This technique also permits the separation of signals modulated at different frequencies, thereby enabling simultaneous detection of two or more signals originating from different sources. We accomplish this by splitting the amplified signal and passing it through an equal number of lock-in amplifiers, each of which demodulates the signal with the appropriate reference frequency.

E. Trade-Offs

Among the desired features of the new design are a short acquisition time and the ability to measure low light levels so as to provide the large dynamic range needed for our measurements—two contradictory demands that have to be traded off. The effectiveness of a lock-in amplifier at recovering a signal buried in noise is determined by the choice of the cutoff frequency of the postdetection filter. A low cutoff frequency, although improving the signal-to-noise ratio, implies a long settling time, thereby reducing the sampling rate. On the other hand, with a wider passband the filter settles faster, but at the expense of reduced noise rejection. To achieve high data sampling rates, we sought to minimize the noise level produced by the PD and amplification electronics, thereby allowing us to use a relatively large postdetection bandwidth. Our final design uses a fourth-order Bessel low-pass filter with a cutoff frequency of $f_{3\mathrm{dB}} = 140$ Hz (corresponding to detection bandwidth of 280 Hz), as this type provides the fastest settling time at a given bandwidth. This allows for data sampling rates in the 100-Hz range (see Subsection 4.C) and provides sufficient isolation of 44 dB for a 1-kHz signal separation between the modulated sources.

F. Parallel Detection

A CCD array provides a convenient approach to parallel data sampling. To achieve an equivalent measurement using the PD's, we use S/H techniques. When triggered, the circuit rapidly samples (within 10 μs) the prevailing signal level, which is retained by a capacitor for a certain amount of time. The retention time is determined by inevitable losses that lead to current leakages at the storage capacitor, and therefore to a voltage droop over time. In our configuration, the droop rate is of the order of 0.7 mV/s, which allows for a readout time of up to 10 ms, keeping errors below 1% even for the weakest signals expected. Concerns that arise when active elements (active filters, S/H) are used subsequently to demodulate a signal are the nonnegligible offset voltages (several millivolts) and offset-voltage drifts that can occur. These sources of error can be eliminated by performance of dark current measurements.

G. Other Features

Because we use lock-in detection, the phase of the reference signal must be adjustable with respect to the signal modulation so as to maximize the output signal. To accomplish this, we developed a digital phase shifter based on a digital phase-locked loop, together with a timing circuit that allows shifting of the reference phase in increments of 1.8°. In addition to its excellent stability with respect to phase and duty cycle, and its linear operation over 360°, this design permits convenient computer control. Furthermore, the phase shift of this circuit does not vary with frequency (although, of course, the signal phase usually is frequency dependent). Finally, because the phase shifter is TTL compatible, the unit is not committed to any particular laser driver design.

H. System Timing

To achieve parallel readout of all detector channels, we use a 64-channel peripheral component interconnect data-acquisition board (National Instruments Model PCI-6033E) containing a 16-bit digital-to-analog converter and selectable input gains ($1\times$–$100\times$) provided by an onboard programmable gain instrumentation amplifier allowing for an actual digital resolution of up to 22.9 μV (single point) and an absolute accuracy up to 18.1 μV (single point). We chose this approach as a cost-effective, easy-to-scale, high-precision solution for our needs. This board is fully compatible with LabVIEW software (National Instruments), thus facilitating instrument control. The nominal multiplexing rate is 100 kHz, which leads to a minimum channel dwell time of 10 μs. This value does not take into account the additional settling time of the programmable gain instrumentation amplifier, which reduces the effective sampling rate and can occur when the input gain is changed. Assuming a channel settling time of 100 μs (worst case), a full sweep over all 64 channels (e.g., 32 detectors at two wavelengths) would require 6.4 ms, a duration that is comparable with the settling time of the postdetection filter and determines the minimum source dwell time. Thus use of the S/H circuit allows us to read out the detector signal while the source is being moved to the next fiber position. Accordingly, the minimum data-acquisition interval is equal to the greater of these two time delays, if we assume that the slew time for the source is essentially zero. Although this cannot be accomplished with one optical demultiplexing driver, in principle it can be achieved with two operated synchronously, so that when one driver walks onto a transmitting fiber, the other is moving off. In addition, the time re-

quired for reading the S/H circuit can be decreased proportionally by use of more than one analog-to-digital board. Between the two strategies, we are confident that the limiting time factor can be restricted to basically the settling time required for the postdetection filter, and therefore we expect to achieve synchronized source demultiplexing and data sampling rates for a multichannel system of the order of 150 Hz.

4. Results

A. Calibration Studies

To reiterate, the motivation guiding our derived calibration schemes was to not only account for the expected variable coupling efficiencies for each measuring channel but to accomplish this using the same testing configuration employed in actual measurements and to provide for statistical measures that facilitate system troubleshooting. We explored this for two different measuring wavelengths and two different homogeneous media. The target medium used was a latex laboratory glove filled with 500 ml of 1% or 2% Intralipid (IL). We chose a glove instead of a solid vessel as a container in an effort to more closely approximately the type of deformable boundaries encountered with tissue. In other studies we repeated the described measures using a solid vessel and obtained similar results. When we brought the iris measuring head in contact with the glove, the arbitrary initial geometry of the glove was constrained to a cylindrical shape within ~3 cm above and below the plane of measurement so that our assumption of a circular geometry was justified. For each test case explored, we performed parallel optical measurements for each of the 18 source fibers, producing an 18×18 data set.

We then performed an analysis of the measured values by solving Eq. (4) to derive estimates of the coefficients in the **S**, **M**, and **D** matrices, using the second of the above-outlined algorithms. Based on the imposed symmetry of the phantom medium, several predictions can be made from our model regarding the structure of the derived coefficient values and their sensitivity, or lack thereof, to experimental conditions.

For example, the model predicts that only the elements of **M** will vary with the composition of the phantom, whereas those of **S** and **D** matrices will not. Furthermore, **S** should exhibit a greater dependence on the physical source than either **M** or **D** as different incoupling efficiencies will occur because of expected differences in alignment of the different wavelength sources. These expectations are borne out in results shown in Figs. 9–11. Figure 9 is a plot of the calculated mean values for the coupling factors d_j versus the detector number, normalized to the maximum value observed. Inspection reveals that, although there are significant variations among the coupling efficiencies for different detectors (up to almost 50%), d_j at a particular position is largely independent of the background optical properties and wavelength.

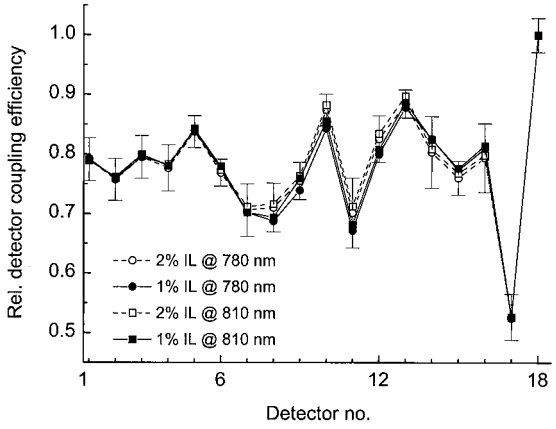

Fig. 9. Plot of mean relative detector coupling efficiencies d_j versus detector number j, as calculated from phantom studies for two values of IL concentration at two wavelengths. Each data point represents the mean value according to Eq. (4). Error bars indicate the standard deviations for one set of data.

The error bars indicate the sample standard deviations, which for clarity are shown for only one data set (1% IL at 780 nm). The corresponding values of s_i are plotted in Fig. 10. Inspection shows that, whereas s_i is very much a function of i, it is also only weakly dependent on the composition of the scattering medium but does show the expected dependence on the physical source. It is plausible that this dependence also is responsible for the variance in s_i being somewhat greater than that observed for d_j.

As a check on the calibration scheme, we also directly measured the relative s_i values experimentally by removing the phantom from the iris and measuring the light power at each end of the source fibers with a powermeter and determined that the measured values coincided well with the calculated source coupling efficiencies. We note that, although doable, this approach is not optimal for practical studies, as it introduces a change in the measuring

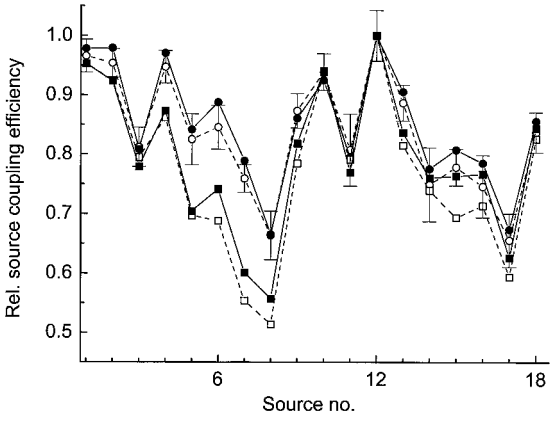

Fig. 10. Plot of mean relative source coupling efficiencies s_i versus detector number i, as calculated from phantom studies for two values of IL concentration at two wavelengths. Error bars indicate the sample standard deviations for one set of data. Symbols are the same as in Fig. 9.

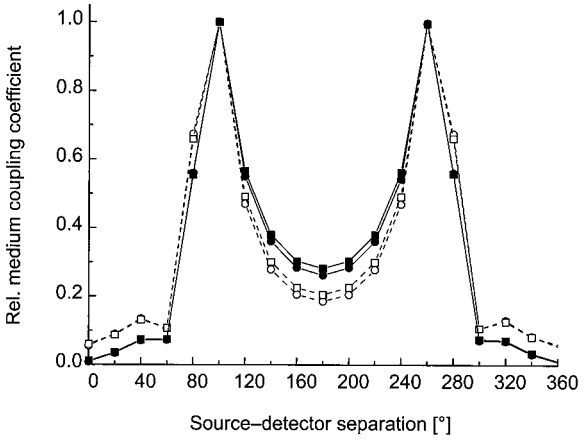

Fig. 11. Plot of the matrix elements m_{ji} versus the source–detector separation angle for two values of IL concentration at two wavelengths. Symbols are the same as in Fig. 9.

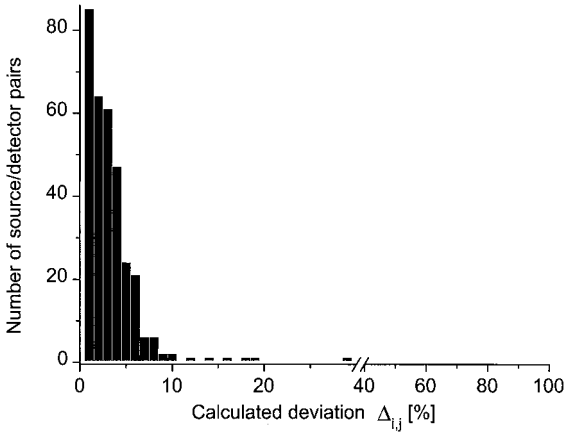

Fig. 12. Histogram indicating the number of source–detector pairs (out of a total of 324) for which the calculated detector response lies within a certain deviation Δ_{ji} from the measured value.

setup. In other studies we measured the within-day and day-to-day stability of the computed coupling coefficients, using various (solid, liquid) homogeneous phantoms. Results obtained demonstrated that in all cases repeatable results were obtained [i.e., coefficient of variation was $<1\%$ and 4%, respectively ($n = 6$)].

Results in Fig. 11 show the expected dependence of the structure of the **M** matrix on the composition and geometry of the target. In the case of a symmetric medium, the derived m_{ij} values should vary in a symmetric fashion about any one source. Inspection shows that, although symmetric, the overall shape of the response curve is complex. Note that the important feature here is the symmetry and not the shape of the function, as the latter depends on the target optical properties and attenuation values of the ND filters used in the variable attenuator assembly. Also seen in Fig. 11 is an expected dependence of the elements of m_{ij} on the IL concentration (i.e., the more concentrated suspension transmits a smaller fraction of the incident light, and backreflects a larger fraction, than does the more diluted suspension). These findings increase our confidence in the validity of the three-factor model [Eq. (3)] and in the method used to separate the factors.

As a further analysis, we calculated the percentage deviation of the modeled detector response from the actual readings according to

$$\Delta_{ij} = 100\,\frac{r_{ij} - n s_i m_{ij} d_j}{r_{ij}}. \tag{10}$$

Here Δ_{ij} is the deviation of the reading r_{ij} from the model value $s_i m_{ji} d_j$, and n is a normalization constant defined as

$$n = \sum_{i,j} r_{ij} \Big/ \sum_{i,j} s_i m_{ij} d_j.$$

It is necessary to introduce this scaling factor, because the nonzero elements of the matrices are normalized to each parameter's (s, d, m) maximum value. Figure 12 shows a histogram illustrating the number of source–detector pairs for which the relative error is within the range indicated on the abscissa. The results show that, when we use the computed coefficients, 93% of the calculated values are within 6% of the corresponding measured detector readings. Because every Δ_{ij} can be attributed to a particular source–detector pair, unusually large Δ_{ij} values, should they occur, can be interpreted as indicators of some type of system error or misalignment, thus providing an objective reliability check.

Overall, the described calibration method represents a simple and robust scheme that permits accurate assessment of coupling losses occurring through the measuring system under the same conditions as are used for experimental studies. In addition, it simultaneously provides statistical measures that are important the monitoring of system performance and reliability. In Subsection 4.B we show representative results from dynamic studies obtained with the above-described instrumentation.

B. Imaging of Dynamic Features in Dense-Scattering Media

To illustrate the quality of imaging information derivable by use of the described instrumentation, we performed a time-series tomographic measurement on a dynamic tissue phantom. A schematic of the setup is shown in Fig. 13. The test medium consisted of a hollow cylindrical vessel composed of white Delrin filled with 500 ml of 2% vol/vol IL that served as a scattering medium. The dimensions of the vessel were 7.6 cm outside diameter, 7.3 cm inside diameter, and 15 cm in height. Added to this was a thin structure that served to support two stretched latex balloons that were filled with 3 ml of a 50-μM solution of Hb in 2% vol/vol IL. The scattering and absorption coefficients of the background medium were estimated to have μ_s' and μ_a values of $\sim$20 cm^{-1} (Refs. 37–39) and $\sim$0.02 cm^{-1},[40] respectively. The added absorption that is due to Hb at the illumina-

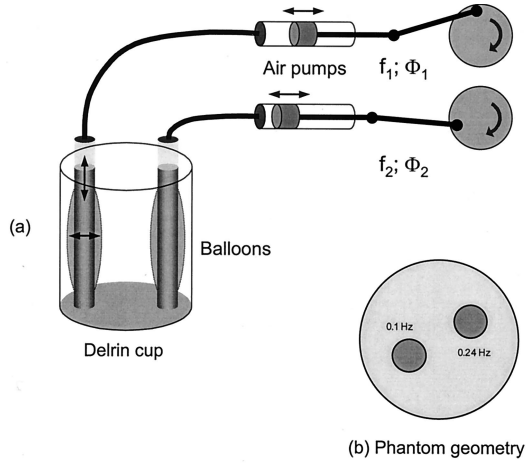

Fig. 13. (a) Schematic of the phantom used to demonstrate dynamic imaging capabilities. (b) Cross section of the target used for experimental studies.

tion wavelength (810 nm) is approximately 0.04 cm^{-1}.[41,42]

Positioned above each balloon was a 5-ml syringe filled with the Hb–IL suspension, serving as a reservoir. The balloons were made to pulsate, one at 0.1 Hz and the other at 0.24 Hz, by pneumatic displacement. This had the effect of rhythmically changing their diameters from ~7 to ~9 mm, corresponding to a maximum variation in balloon volume of approximately 1 ml. The forcing frequencies used, although lower than the typical cardiac and respiratory frequencies observed at rest, did have approximately the correct ratio. For each of six source positions (60° separation), we performed simultaneous measurements at 18 detector locations at a rate of 4 Hz over a 60-s time period, using the iris imaging head and following the protocol outlined in Fig. 6.

From each data set (6 sources, 18 detectors) a cross-sectional image representing one time point of the series was reconstructed. Images were reconstructed with a diffusion-based perturbation solver[43,44] that used a conjugate gradient descent algorithm and extended Dirichlet boundary conditions. Input values for each source–detector pair at each time point were based on the relative change from the time-averaged mean value. Reconstructions were limited to the first-order Born solution, with a maximum of 2000 conjugate gradient descent iterations. This approach has the merit of relatively fast reconstruction [O(1 min) on a SGI Origin 200 workstation with R10000 CPU), which is desirable when one is obtaining an image series containing hundreds to thousands of individually reconstructed images.

Figure 14 shows the images recovered from detector readings collected at two different time points when data were analyzed as variations about the temporal mean value.[44] When evaluated in this manner, detector variations about the mean yield positive and negative deflections in the mapped optical quantities. Although indicating the presence of

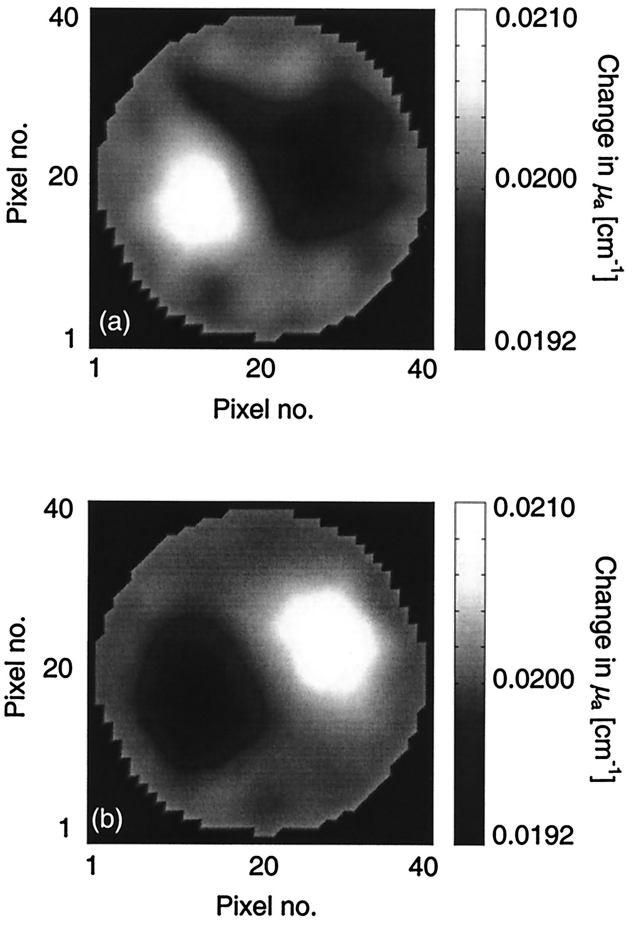

Fig. 14. Reconstructed images showing snapshots of dynamic phantom at different times: (a) 2 s, (b) 5 s.

temporal variations, these results do not provide specific measures of the dynamic behavior. This can be obtained from evaluation of the temporal Fourier transform of the computed image series. These results are presented in Fig. 15. Shown here are maps of the Fourier-transform amplitudes computed at the two beat frequencies. Inspection reveals nearly complete spatiotemporal resolution of the two objects. Compared with Fig. 14, these images have improved edge resolution and >100× improvement in contrast over the background. Because similar differences in the ratio of the beat frequencies exist for vascular structures, extension of these results to *in vivo* measurements suggests that similar spatiotemporal resolution of the arteries from the veins and microvessels might be possible. This capability has been demonstrated in a series of recent reports.[45–47] Next we show results documenting the measured performance features of the new system under construction.

C. Silicon-Photodiode-Based System Performance

In Table 1 we show the performance characteristics of a single-channel prototype containing one lock-in amplifier based on the design described in Section 3. We measured the settling time of the detector by

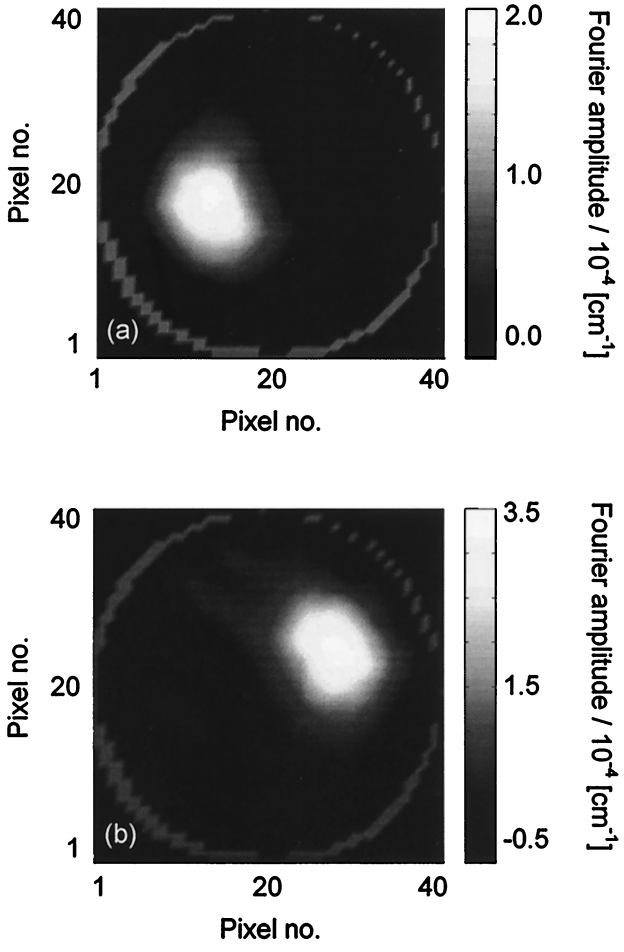

Fig. 15. Amplitude maps of the Fourier transform of the reconstructed image time series at two beat frequencies: (a) 0.1 Hz, (b) 0.24 Hz.

modulating the 5-kHz source-driving frequency with a rectangular signal (~50 Hz), thereby inducing fast changes in the average light power. We could then judge the temporal response of the postdetector filter to a transient change in light power by monitoring the output signal. We observed a slight overshoot with a maximum at 5 ms that settled to within <1% of the final signal level within 7 ms. This shows that, depending on the desired accuracy, data-acquisition rates of the order of 150 Hz are achievable.

Table 1. Performance Characteristics of the SiPD Detector Module

Parameter	Value
Modulation frequency	5–10 kHz
Detector settling time	5–10 ms (5%–<1%)
Data-acquisition rate	150 Hz
Noise-equivalent power	~10 pW (rms)
Dynamic range	1:10^9 (180 dB)
Long-term stability	~1% over 30 min
Background light suppression	Daylight signal ~3× dark noise (at highest gain)

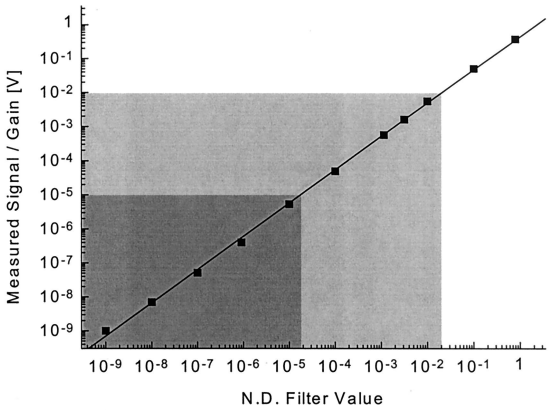

Fig. 16. Measurement of dynamic performance of the detector channel.

The noise-equivalent power over the detection bandwidth of the detector module was estimated as somewhat lower than 10 pW. We evaluated this by shielding the PD and recording the rms noise voltage at the highest gain setting. We then calculated the associated light power level by accounting for the known sensitivity of the PD and the amplification factors used in the system. This noise determines the lower limit of the dynamic range of our detector circuit. The upper limit is the signal level at which the PD begins to show saturation effects, which occur at intensities of approximately 10 mW (in the 800-nm region). This leads to an overall linear range of 9 orders of magnitude.

Figure 16 shows the results of measurements that were carried out to determine the linear dynamic range of the system. We achieved variations in light levels by introducing calibrated ND filters between an amplitude-modulated laser source (~10 mW) and the photodetector. Plotted in Fig. 16 is the ratio of measured signal voltage to the corresponding gain factor employed versus the nominal optical density value of the filters. The different shading levels in the figure correspond to the three different gain settings used in the measurement. We adopted this relatively simple method because no accurate reference detector having sufficient dynamic range was available. Although this limits our ability to make specific statements regarding linearity, the results obtained would strongly indicate that the measuring system is in fact linear over its entire measuring range [i.e., 10^9 (180 dB)].

We further experimentally evaluated the influence of gain adjustments on the reproducibility of measurements. The error introduced (coefficient of variation) in the measured light intensity when the gain setting was changed by a factor of 10^3 and 10^6 is <1%. This finding is not unexpected, because the two gain switching mechanisms employed provide high-gain accuracy (<1%) and have low temperature coefficients (<100 parts per million/°C). In other studies

we determined the long-term stability of measurement to thermal variations. We observed that the measured signal deviated by <1% over a time frame of up to 1 h.

We also quantified the rejection of ambient light. As expected, most disturbing is light emitted by fluorescent bulbs, which contain not only the nominal 120-Hz modulation but also a significant amount of power in its overtones. Because we perform lock-in detection with a relatively large filter bandwidth, direct exposure of the PD to fluorescent room light compromises measurements at the most sensitive gain setting. However, this effect is considerably reduced when the PD instead receives light that emerges from an actual target by way of the measuring heads. Much less disturbing is daylight or light from an incandescent tungsten lamp. When the detector is exposed to daylight coming through a window, the signal level increases twofold to threefold over the dark-noise level at the highest gain setting. In practice we would expect this to be significantly suppressed, as the only source of ambient light reaching the detector would be from the receiving fibers at the measuring head, which would be strongly shielded by the target coming into contact with the fibers.

5. Discussion

Two features that distinguish optical tomography from most other imaging modalities and that have an impact on instrumentation design are the need for contact measurements and the underlying reactivity of the principal contrast feature (i.e., Hb). Our approach to meeting these requirements has been to adopt various design features that permit fast collection of tomographic data from media having arbitrary geometries. Acquisition of time-varying data in a tomographic modality opens a new door regarding the information retrievable from tissue by optical tomography.[46] Until now, imaging studies have been restricted mainly to the evaluation of seemingly static contrast features arising from, for example, spatially varying Hb content and its oxygenation state.[3] In addition to these measures, however, analysis of time-varying data can provide a wealth of information regarding the perfusion state of tissue, among other measures. In fact, for many clinical situations, the latter is the more significant issue. Most encouraging is a recent demonstration by our group[46] that dynamic features of a dense-scattering medium can be recovered with much greater accuracy and improved contrast than is seen in image maps of static contrast features.

Naturally, investigation of these properties requires acquisition of time-varying data. Our CCD-based system is capable of a 4-Hz parallel measurement. For single-wavelength studies, this is sufficiently fast to accurately monitor a cardiac signal.[45] To achieve optimal image quality, a multisource measurement should be adopted. Also important is the timing sequence of the illumination scheme. Two approaches are possible. Sequential source measurements (our current capability) are adequate for the monitoring of dynamic behavior, provided that the frequency and phase response of the system is reproducible. This is easily accomplished for phantom studies, and, as shown in Fig. 15, high-quality images can be reconstructed. It may also be adequate for certain physiological studies, in particular for cases involving an applied stimulus or where the measurement can be synchronized with a particular frequency (e.g., the cardiac signal). However, it is well known that the temporal behavior of the vasculature is highly variable, and probably chaotic, even at rest.[48] Investigation of these properties will require multisource measurements with parallel detection on a time frame that is fast compared with the naturally occurring vascular frequencies. This has been the goal of our SiPD-based system. In Subsection 5.A we discuss a range of issues influencing our approach to instrument design, particularly in relation to recently described measuring systems.

A. Imaging Head Design

1. Pad

The need for direct contact between optical fibers and the target implies a necessity for use of geometrically adaptive measuring heads. A conforming device similar to the imaging pad should allow for good contact between the fiber optics and the tissue surface. Because the external geometry of tissue is usually irregular, it seems likely that this approach would limit specific knowledge of the position of the optical fibers. As shown previously by Boas *et al.*,[49] uncertainty of this type may strongly influence sensitivity measures of internal structures. The importance of this effect, however, can be expected to depend on how the measurement data are treated. For example, efforts to define absolute coefficient values will likely be much more sensitive to this uncertainty than would corresponding measures of relative changes.[43,44]

The imaging pad was designed to permit backreflection measurements from structures too thick for transmission studies. Although some groups recently have described devices superficially similar to ours, it is useful to point out the unique features of our design. Usually, when adopting a sensor array having a flat geometry, one would think of imaging planes running parallel to the surface. This approach was adopted by Yamashita *et al.*,[6] who chose a 2-D array of equidistantly alternating sources and detectors with optimized sensitivity to a plane running underneath the human scalp to allow for dynamic topography studies of the cerebral cortex. Using a similar design, Siegel *et al.*[1] produced an image of a rat brain with an image slice thickness of 1 mm.

Contrary to these approaches, we seek to establish imaging planes that run perpendicular to the tissue

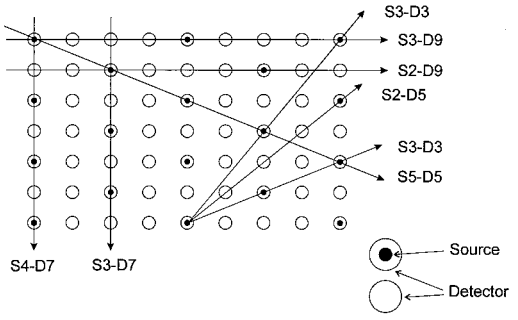

Fig. 17. Schematic drawing of the arrangement of source and detector fibers on the pad.

surface. Previously, Chang *et al.*[50] described a reconstruction method capable of providing such views. A straight line of multiple sources and detectors on a flat surface can be regarded as a segment of an iris of infinite diameter. Based on this concept, when a padlike imaging head is designed, it is desirable to maximize the source–detector density along as many imaging planes as possible. The alternating 3×2 source density along the long axis of the array permits reconstruction of up to 28 independent 2-D images involving a minimum of three fibers lying within a plane. These fall into two classes: those parallel to the major axes and those that lie along a diagonal (see Fig. 17). It is convenient to identify these in accordance to their source (S) and detector (D) density; the nomenclature that we devised for this purpose is $(x)[Sn_s - Dn_d]$, where x = number of imaging planes and n_s and n_d are the numbers of fibers of each type lying within a plane. Parallel to the major axes we find (3)[S4-D7], (2)[S3-D7], (3)[S2-D9], and (4)[S3-D9]. Diagonal to the axes we find (4)[S5-D5]. Originating from the center positions of the outermost nine-fiber arrays we also find (4)[S2-D5], (4)[S3-D3] (consisting entirely of adjacent fibers), and (4)[S3-D3] (composed of nonadjacent fibers). The advantage of this approach is that rather than directly computing a full three-dimensional (3-D) reconstruction, a set of intersecting 2-D planes can be computed instead, thereby providing a pseudo-3-D image. Another advantage of this scheme is that it readily permits use of parallel codes[51] and allows the selection of specific regions for iterative computations without one having to consider the entire volume.

The symmetric geometry of the hemisphere, like that of the pad, is suitable for construction of pseudo-3-D images from intersecting image planes. The number of such planes depends on the configuration of the hemisphere–irises unit employed for a particular set of measurements. For the unit depicted in Fig. 5, and with the same nomenclature as before, we have (2)[S8-D8] image planes parallel to the chest wall, (4)[S7-D7] planes that are perpendicular to the chest wall and that all intersect in the ventral–dorsal axis, and (4)[S5-D5] planes that are oblique to the chest wall. Still other imaging planes are present involving fewer source–detector pairs.

2. *Adjustable-Size, Fixed-Geometry Measuring Heads*

The two other imaging head designs that we adopted (i.e., the iris and folding hemisphere) permit gentle deformation of certain tissue structures to specific geometries. These have the advantage of accommodating a range of tissue sizes while simultaneously retaining specific knowledge of the fiber positions. These devices also are effective in stabilizing the tissue against motion artifacts. The iris design appears well suited to the investigation of tissues having an approximately cylindrical geometry (e.g., the limbs). If desired, volumetric imaging can be achieved by a stacked iris configuration. This approach could also be adopted for imaging studies of the breast. A nearly cylindrical geometry could be imposed on the breast by gentle compression in the ventral–dorsal direction while several iris units are simultaneously brought into contact with the tissue.

Preservation of the natural contour of the breast is possible with the folding hemisphere. As indicated, we found that, depending on breast size, additional folding structures may be required to permit investigations of the breast near the chest wall. When the hemisphere and folding iris units are attached to appropriate translation devices, the measuring head design can be made to accommodate essentially any breast size.

3. *Other Designs*

We recognize that the design of our measuring devices is more complex than others, especially as they relate to possible use in breast studies. Other devices that have been reported include ones that produce mild planar compression,[52] a fixed cup geometry,[7] and a circular array similar in function to the iris.[2,53] Although simpler in design, each introduces limitations that we believe render it less suitable than ours for examination of the breast.

The simplest design is planar compression. This is the scheme adopted in x-ray mammography. Apart from stabilizing against motion artifacts, compression is used in x-ray studies to improve image resolution. Recently we have shown that, contrary to one's intuition, this effect does not always extend to optical imaging studies.[13] In particular, we have shown that, although decreasing the optical thickness of a medium (e.g., by compression) improves signal levels, sensitivity to included objects and their edge resolution is frequently reduced.[13] As described elsewhere,[54] the reasons for this are complex, but basically are related to the fact that sensitivity and resolution in a scattering medium are strongly dependent on the properties of the weighting function. The latter is influenced in turn both by the background optical properties and by the average optical path length. Compression can also be expected to alter both tissue blood volume and the vascular response of the tissue. Depending on the measurement, this may or may not be desirable.

Colak *et al.*[7] have introduced a fixed cup geometry

for breast studies. The obvious difficulty here is that breast size can vary considerably. For breast sizes smaller than the cup geometry, optical coupling is retained when an index-matching scattering medium is introduced (e.g., Intralipid). For breasts of larger size, the fixed geometry limits the volume of tissue that can be examined. For most clinical investigations, this limitation would seem unacceptable. The folding hemisphere design described here avoids this, but it does necessarily affect the measurement density. The impact of this on image quality is a subject for further investigation.

Pogue *et al.*[2] and Zhao *et al.*[53] have reported results obtained by using circularly adjustable measuring heads. These designs are functionally similar to the iris described here, but do not adopt a parallel measurement.

B. Illumination and Detection Scheme

A key goal of our instrumentation design has been to achieve fast source demultiplexing coupled to parallel data acquisition and a large dynamic range. The need for speed originates from the desire to monitor dynamic events. The dynamic range requirement is based on the importance of achieving a broad view angle, a parameter significant for image reconstruction. In the absence of this, it is difficult if not impossible to differentiate features near the surface from those at greater depths. This is especially true in the case of dc illumination.[12] Related to acquisition speed is the need for multiwavelength measurements. This is important for tissue studies, where it is useful to distinguish hemodynamic processes that involve local variations in blood volume from those resulting from changes in blood oxygenation.

In fact, it is possible for one to achieve what amounts to an infinite source scanning speed by illuminating a target at multiple source positions simultaneously. Differentiation of one source from another can be made by lock-in detection methods. This parallel-source, parallel-detector strategy is the approach taken by Siegel *et al.*[1] and Yamashita *et al.*[6] Although seemingly elegant, there are two interrelated difficulties with measurement schemes of this type that we believe ultimately will make them less desirable for tissue studies than the serial-source, parallel-detector scheme outlined in Section 3. One difficulty is that as the interval between successive modulation frequencies decreases with an increasing number of sources, so too does the detection band width that is available for isolating the signals. In the time domain, this corresponds to longer detector settling times and therefore reduced acquisition rates. This trade-off has served to limit the parallel acquisition speed reported by Yamashita *et al.*[6] to 2 Hz. Although one could obtain faster acquisition rates by increasing the detection bandwidth, this could, depending on the number of sources employed, lead to a requirement for employing rather high modulation frequencies for some of the sources. However, it is desirable to avoid high-frequency modulation ($>$30 kHz) because of the expectation of bandwidth limitations for a high-gain transimpedance amplifier, which can lead to loss of sensitivity.

Although the reported acquisition speed[6] may be adequate for some applications, the trade-offs associated with simultaneous multisource illumination extend beyond this issue. Perhaps of greater concern is the expectation that this approach can greatly restrict the dynamic range of measurement. The reason for this is that for any given gain setting there is a finite range between the noise limit of measurement and the signal level that will saturate the sensing electronics (typically 4 decades). Within this range, the total photocurrent produced is proportional to the linear sum of light reaching a detector from all sources. Thus the presence of additional sources limits the maximum signal level measurable from any given source. In practice this means that it is not possible for a given detector to measure the weak signal originating from distant sources if another source is located nearby. To do so would require an increase in the detector gain, which would immediately lead to saturation of the electronics because of the contribution from the nearby source.

In the case of our SiPD-based system, our approach to addressing these trade-offs has been to limit use of lock-in detection methods to performance of simultaneous multiwavelength measurements at a single source position. Because light originates from only one location at any one time, we have the opportunity to adjust the gain settings for detectors in relation to their distance from the source, which allows use of an extremely large dynamic measurement range (180 dB), as shown in Fig. 16. Using fast-settling lock-in amplifiers with a relatively large detection bandwidth of 280 Hz permits us to achieve short settling times and hence high acquisition rates.

A fast detector is necessary but is not by itself sufficient to ensure rapid data acquisition. To achieve this, it is also necessary that the time required to adjust the gain setting be much less than the settling time of the lock-in amplifiers. It is likely that this capability cannot be achieved with optomechanical methods of the type employed in our CCD-based system (i.e., variable attenuator, Fig. 2). Instead we have introduced TTL-controllable gain adjustment for each detector channel. The switching time for these devices is $<$0.5 ms, which is sufficiently fast to allow for on-the-fly adjustment of the gain under computer control, thereby permitting fast source multiplexing. The latter is achieved by mechanical means with a high-performance dc brushless servomotor.

As mentioned above, lock-in detection methods also serve to conveniently filter out the interference from ambient light. Our CCD-based instrument lacks this feature, and for this reason considerable care must be taken to exclude ambient light from entering the optical path. In practice, this means that each component of the system must be heavily shielded. Although inconvenient, the current design is nevertheless capable of providing excellent spatiotemporal resolution of dynamic features, as shown in Fig. 15.

It should be pointed out that performance studies for the SiPD-based system have been conducted thus far on only a single prototype channel. Our next steps will be verification of the expected overall performance of a multichannel instrument and the integration of the detection scheme, measurement head, and input coupler into a single functioning system.

C. Further Improvements

We have already pointed out that the short acquisition time, which was a design priority, leads to tradeoffs in detection sensitivity. To optimize detection speed, our SiPD-based system is less sensitive than the currently used CCD-based instrument. Although we are confident that the SiPD detection scheme will prove useful in a wealth of applications, there nevertheless could be cases in which it has insufficient sensitivity for certain applications (e.g., imaging of large breasts). In these situations, use of larger-diameter detector fibers together with added focusing optics between the fiber end and detector should increase detection sensitivity. This would permit use of SiPD's having smaller sensor areas, which can be expected to reduce electric noise because their junction capacitance will be smaller.[36] As techniques of this type serve to optimize light collection, they should not limit achievable detection speeds. On the other hand, should it prove desirable to relax this feature, then improved sensitivity through improved noise reduction can be achieved through the simple expedient of lowering the cutoff frequency of the postdetection filter. This will improve the signal-to-noise ratio in proportion to the square root of the decrease in the detection bandwidth (or the increase in acquisition time). Hence, if the acquisition time were increased to 0.7 s, it would improve measurement sensitivity by a factor of 10.

D. System Calibration

One goal of calibration is to distinguish variations in optical signals caused by factors attributable to the target medium from those arising from variable transmission efficiencies in the instrument. In our system, variations in channel efficiency are attributable to losses caused by the varying coupling efficiencies at the different optical interfaces (e.g., coupling of light into the fibers, delivery of light into the target, collection of light from the target, and conduction of this light to the detector array), as well as transfer losses that are due to fiber bending. Of these, the most difficult loss terms to identify are those associated with the fiber-to-tissue incoupling and tissue-to-fiber outcoupling efficiencies. This concern exists because of the expected sensitivity of coupling efficiency to the precise alignment of the fibers at the tissue interface, which will depend on small variations in the external tissue geometry, its plasticity, and other factors influencing surface conditions (e.g., moisture, texture, hair). Although precise measurement of these values seems unlikely, our use of geometrically adaptive but rigid imaging heads should serve to minimize variation in these values among the fibers.

Another consideration that we took in devising the described calibration protocol was that the calibration measurements should be made with all components of the instrument, particularly all optical fiber ends, in the fully assembled state that will be used for the planned physiological investigations. This is especially important for clinical investigations where a variety of sources of error can occur because of unexpected instrument failure, operator error, etc., that may not be detected should alternate calibration strategies be implemented. Still another goal was to adopt a scheme that does not depend on any assumptions concerning the physics of photon transport. The only assumption we make in this regard is that the incoupling and outcoupling efficiencies for our phantom apply to our target medium. In practice, it can be expected that the actual values will differ by some offset. The influence of this on the accuracy of recovered images will likely depend on how the measurement data are treated (see Refs. 43 and 44). Still another feature of our calibration scheme that we believe may have considerable practical value is its ability to derive statistical data associated with the estimates of the coefficient values. This not only permits improved estimation of these values, but also provides insight on system performance that is useful for troubleshooting applications.

The calibration procedures that were presented above also have several other features worth mentioning. One is that, although the first algorithm for separating the elements of matrices **S**, **M**, and **D** requires that **M**, and consequently the calibrating target medium, have a specific structure, the second does not. The IPF-based method can in principle be applied to a detector reading matrix **R** obtained with any medium whatever, provided that the structure that **M** should possess for said medium is known. For an arbitrary heterogeneous medium it is not reasonable to expect that this knowledge will be available, as it would be tantamount to one knowing the result of a measurement before it is performed. Another potentially valuable property of the model is the possibility that it can be extended in ways that take account of the anticipated effects of different types of system failure. For example, cross talk between channels would be expected to introduce nonzero off-diagonal elements into **S** or **D**. Which matrix is affected will depend on which physical component of the instrument is responsible for the cross contamination. This is a nontrivial concern, given the large dynamic range of the measurements we seek to perform. Recently commenced model studies on the impact of the different type of deviations from the three-factor model on the result obtained with each algorithm will determine the extent to which different sources of instrument failure can be identified and distinguished in this manner.

Finally, proper system calibration should allow for a more accurate assessment of absolute changes in the time-varying optical properties of a target me-

dium. In the absence of this, only within-channel variations can be studied reliably. However, even with this limitation, as we have recently shown,[47] much useful information is nevertheless retrievable from tissue studies.

This research was supported in part by National Institutes of Health grant RO1-CA 66184 and by the New York State Science and Technology Foundation.

References

1. A. M. Siegel, J. J. A. Marota, and D. A. Boas, "Design and evaluation of a continuous-wave diffuse optical tomography system," Opt. Exp. **4,** 287–298 (1999).
2. B. W. Pogue, M. Testorf, T. Mcbride, U. Osterberg, and K. Paulsen, "Instrumentation and design of a frequency-domain diffuse optical tomography imager for breast cancer detection," Opt. Exp. **1,** 391–403 (1997).
3. B. Chance, "Near-infrared images using continuous, phase-modulated, and pulsed light with quantitation of blood and blood oxygenation," in *Advances in Optical Biopsy and Optical Mammography* R. R. Alfano, ed., Ann. N. Y. Acad. Sci. **838,** 29–45 (1998).
4. R. L. Barbour, R. Andronica, Q. Sha, H. L. Graber, and I. Soller, "Development and evaluation of the IRIS-OPTIscanner, a general-purpose optical tomographic imaging system," in *Advances in Optical Imaging and Photon Migration*, J. G. Fujimoto and M. S. Patterson, eds., Vol. 21 of OSA Trends in Optics and Photonics (Optical Society of America, Washington, D.C., 1998), pp. 251–255.
5. J. C. Hebden, F. E. W. Schmidt, M. E. Fry, M. Schweiger, E. C. Hillman, D. T. Delpy, and S. R. Arridge, "Simultaneous reconstruction of absorption and scattering images by multichannel measurement of purely temporal data," Opt. Lett. **24,** 534–536 (1999).
6. Y. Yamashita, A. Maki, and H. Koizumi, "Measurement system for noninvasive dynamic optical topography," J. Biomed. Opt. **4,** 414–417 (1999).
7. S. B. Colak, D. G. Papaioannou, G. W. 't Hooft, M. B. van der Mark, H. Schomberg, J. C. J. Paasschens, J. B. M. Melissen, and N. A. A. J. van Asten, "Tomographic image reconstruction from optical projections in light-diffusing media," Appl. Opt. **36,** 180–213 (1997).
8. H. Rinneberg, D. Grosenick, H. Wabnitz, H. Danlewski, K. Moesta, and P. Schlag, "Time-domain optical mammography: results on phantoms, healthy volunteers, and patients," in *Advances in Optical Imaging and Photon Migration*, J. G. Fujimoto and M. S. Patterson, eds., Vol. 21 of OSA Trends in Optics and Photonics (Optical Society of America, Washington, D.C., 1998), pp. 278–280.
9. R. J. Grable, P. D. Rohler, and K. L. A. Sastry, "Optical tomography breast imaging," in *Optical Tomography and Spectroscopy of Tissue: Theory, Instrumentation, Model, and Human Studies II*, B. Chance and R. R. Alfano, eds., Proc. SPIE **2979,** 197–210 (1997).
10. H. Eda, I. Oda, Y. Ito, Y. Wada, Y. Oikawa, Y. Tsunasawa, M. Takada, Y. Tsuchiya, Y. Yamashira, M. Oda, A. Sassaroli, Y. Yamada, and M. Tamura, "Multi-channel time-resolved optical tomographic imaging system," Rev. Sci. Instrum. **70,** 3595–3602 (1999).
11. H. L. Graber, R. L. Barbour, and J. Chang, "Algebraic reconstruction of images of a diffusive medium containing strong absorbers: comparative study of different illumination schemes and the effect of restricted view angle," in *Optical Tomography, Photon Migration, and Spectroscopy of Tissue and Model Media: Theory, Human Studies, and Instrumentation*, B. Chance and R. R. Alfano, eds., Proc. SPIE **2389,** 431–447 (1995).
12. S. R. Arridge and W. R. B. Lionheart, "Nonuniqueness in diffusion-based optical tomography," Opt. Lett. **23,** 882–884 (1998).
13. Y. Pei, F.-B. Lin, and R. L. Barbour, "Modeling of sensitivity and resolution to an included object in homogeneous scattering media and in MRI-derived breast maps," Opt. Exp. **5,** 203–219 (1999).
14. B. W. Pogue, T. O. McBride, U. L. Osterberg, and K. D. Paulsen, "Comparison of imaging geometries for diffuse optical tomography of tissue," Opt. Exp. **4,** 270–286 (1999).
15. A. H. Hielscher, R. E. Alcouffe, and R. L. Barbour, "Comparison of finite-difference transport and diffusion calculations for photon migration in homogeneous and heterogeneous tissues," Phys. Med. Biol. **43,** 1285–1302 (1998).
16. S. R. Arridge, "Optical tomography in medical imaging," Inverse Probl. **15,** 41–93 (1999).
17. S. Conolly, A. Macovski, J. Pauly, J. Schenk, K. K. Kwong, D. A. Chesler, X. Hu, W. Chen, M. Patel, and K. Ugurbil, "Magnetic resonance imaging," in *The Biomedical Engineering Handbook*, 2nd ed., J. D. Bronzino, ed. (CRC Press, Boca Raton, Fla., 2000), Chap. 63.
18. J. T. Bruulsema, J. E. Hayward, T. J. Farrell, M. S. Patterson, L. Heinemann, M. Berger, T. Kochinsky, J. Sandahl-Christiansen, H. Orskov, M. Essenpreiss, G. Schmelzeisen-Redeker, and D. Böcker, "Correlation between blood glucose concentration in diabetics and noninvasively measured tissue optical scattering coefficient," Opt. Lett. **22,** 190–192 (1997).
19. G. Gratton, M. Fabiani, D. Friedman, M. A. Franceschini, S. Fantini, P. Corballis, and E. Gratton, "Rapid changes of optical parameters in the human brain during a tapping task," J. Cogn. Neurosci. **7,** 446–456 (1995).
20. D. A. Boas and A. G. Yodh, "Spatially varying dynamical properties of turbid media probed with diffusing temporal light correlation," J. Opt. Soc. Am. A. **14,** 192–215 (1997).
21. J. B. West, ed., *Best and Taylor's Physiological Basis of Medical Practice*, 11th ed. (Williams and Wilkins, Baltimore, Md., 1985).
22. C. R. Honig, C. L. Odoroff, and J. L. Frierson, "Capillary recruitment in exercise: rate, extent, uniformity and relation to blood flow," Am. J. Physiol. **238,** H31–H42 (1980).
23. Y. Kakihana, M. Kessler, A. Krug, H. Yamada, T. Oda, and N. Yoshimura, "Dynamic changes in intracapillary hemoglobin oxygenation in human skin following various temperature changes," Microvasc. Res. **56,** 104–112 (1998).
24. S. Sundberg and M. Castrén, "Drug- and temperature-induced changes in peripheral circulation measured by laser-Doppler flowmetry and digital-pulse plethysmography," Scand. J. Clin. Lab. Invest. **46,** 359–365 (1986).
25. R. B. King, G. M. Raymond, and J. B. Bassingthwaighte, "Modeling blood flow heterogeneity," Ann. Biomed. Eng. **24,** 352–372 (1996).
26. S. Bertuglia, A. Colantuoni, M. Arnold, and H. Witte, "Dynamic coherence analysis of vasomotion and flow motion in skeletal muscle microcirculation," Microvasc. Res. **52,** 235–244 (1996).
27. J. Ross, Jr., "Structure-function relations in the peripheral circulation," Chap. 6 in Ref. 21.
28. R. Bannister, ed., *Autonomic Failure: A Textbook of Clinical Disorders of the Autonomic Nervous System*, 2nd ed. (Oxford U. Press, London, 1988).
29. R. R. Alfano, S. G. Demos, P. Galland, S. K. Gayen, Y. Guo, P. P. Ho, X. Liang, F. Liu, L. Wang, Q. Z. Wang, and W. B. Wang, "Time-resolved and nonlinear imaging for medical applications," in *Advances in Optical Biopsy and Optical Mammography* R. R. Alfano, ed., Ann. N. Y. Acad. Sci. **838,** 14–28 (1998).
30. V. Chernomordik, D. Hattery, A. H. Gandjbakhche, A. Pifferi,

P. Taroni, A. Torricelli, G. Valentini, R. Cubeddu, and J. C. Hebden, "Quantitative imaging in time-resolved transillumination experiments using time-dependent contrast functions," in *Optical Tomography and Spectroscopy of Tissue III*, B. Chance, R. R. Alfano, and B. J. Tromberg, eds., Proc. SPIE **3597,** 398–402 (1999).
31. C. S. Hoberman, "Reversibly expandable three-dimensional structure," U.S. patent 4,780,344 (25 October 1988).
32. P. J. Rousseeuw, "Robust estimation and identifying outliers," in *Handbook of Statistical Methods for Engineers and Scientists*, H. M. Wadsworth, Jr., ed. (McGraw-Hill, New York, 1990), Chap. 16.
33. Y. M. M. Bishop, S. E. Fienberg, and P. W. Holland, "Maximum likelihood estimates for complete tables," in *Discrete Multivariate Analysis: Theory and Practice* (MIT, Cambridge, Mass., 1991), Chap. 3.
34. E. M. Sevick, J. R. Lakowicz, H. Szmacinski, K. Nowaczyk, and M. L. Johnson, "Frequency domain imaging of absorbers obscured by scattering," J. Photochem. Photobiol. B **16,** 169–185 (1992).
35. "Photodiode monitoring with op amps," Burr-Brown Application Bulletin AB-075 (Burr-Brown Corp., 6730 S. Tucson Blvd., Tucson, Ariz., 1995).
36. "Photodiodes," Catalog No. KPD0001E07 (Hamamatsu Photonics, Bridgewater, N.J. 08807, 1998).
37. H. J. van Staveren, C. J. M. Moes, J. van Marle, S. A. Prahl, and M. J. C. van Gemert, "Light scattering in Intralipid-10% in the wavelength range of 400–1100 nm," Appl. Opt. **30,** 4507–4514 (1991).
38. I. Driver, J. W. Feather, P. R. King, and J. B. Dawson, "The optical properties of aqueous suspensions of Intralipid, a fat emulsion," Phys. Med. Biol. **34,** 1927–1930 (1989).
39. S. T. Flock, S. L. Jacques, B. C. Wilson, W. M. Star, and M. J. C. van Gemert, "Optical properties of Intralipid: a phantom medium for light propagation studies," Lasers Surg. Med. **12,** 510–519 (1992).
40. G. M. Hale and M. R. Querry, "Optical constants of water in the 200-nm to 200-μm wavelength region," Appl. Opt. **12,** 555–563 (1973).
41. O. W. van Assendelft, *Spectrophotometry of Haemoglobin Derivatives* (Royal Vangorcum Ltd., Assen, The Netherlands, 1970).
42. S. Wray, M. Cope, D. T. Delpy, J. S. Wyatt, and E. O. R. Reynolds, "Characterization of the near infrared absorption spectra of cytochrome aa_3 and haemoglobin for the noninvasive monitoring of cerebral oxygenation," Biochim. Biophys. Acta **933,** 184–192 (1988).
43. Y. Pei, "Optical tomographic imaging using finite element method," Ph.D. dissertation (Polytechnic University, Brooklyn, N.Y., 1999).
44. Y. Pei, H. L. Graber, and R. L. Barbour are preparing a manuscript to be called "Influence of systematic errors in reference states on image quality and on stability of derived information for dc optical imaging."
45. R. L. Barbour, H. L. Graber, Y. Pei, S. Zhong, and C. H. Schmitz are preparing a manuscript to be called "Optical tomographic imaging of dynamic features of dense-scattering media."
46. S. Blattman, H. L. Graber, S. Zhong, Y. Pei, J. Hira, I. Arif, and R. L. Barbour, "Imaging of differential reactivity of the vascular tree in the human forearm by optical tomography," in *Biomedical Topical Meetings*, Postconference Digest, Vol. 38 of OSA Trends in Optics and Photonics Series (Optical Society of America, Washington, D.C., 2000), pp. 458–460.
47. R. L. Barbour, S. Blattman, and T. Panetta, "Dynamic optical tomography: a new approach for investigating tissue–vascular coupling in large tissue structures," in *Biomedical Topical Meetings*, Postconference Digest, Vol. 38 of OSA Trends in Optics and Photonics Series (Optical Society of America, Washington, D.C., 2000), pp. 336–338.
48. L. Glass and M. C. Mackey, *From Clocks to Chaos: The Rhythms of Life* (Princeton University, Princeton, N.J., 1988).
49. D. A. Boas, M. A. O'Leary, B. Chance, and A. G. Yodh, "Detection and characterization of optical imhomogeneities with diffuse photon density waves: a signal-to-noise analysis," Appl. Opt. **36,** 75–92 (1997).
50. J. Chang, W. Zhu, Y. Wang, H. L. Graber, and R. L. Barbour, "Regularized progressive expansion algorithm for recovery of scattering media from time-resolved data," J. Opt. Soc. Am. A **14,** 306–312 (1997).
51. S. Bartel, G. Abdoulaev, and A. H. Hielscher, "Parallelization of gradient-based iterative image reconstruction scheme," in *Biomedical Topical Meetings*, Postconference Digest, Vol. 38 of OSA Trends in Optics and Phototonics Series (Optical Society of America, Washington, D.C., 2000), pp. 433–435.
52. S. Nioka, M. Miwa, S. Orel, M. Shnall, M. Haida, S. Zhao, and B. Chance, "Optical imaging of human breast cancer," in *Oxygen Transport to Tissue XVI*, Vol. 361 of Advances in Experimental Medicine and Biology, M. C. Hogan, O. Mathieu-Costello, D. C. Poole, and P. D. Wagner, eds. (Plenum, New York, 1994), pp. 171–179.
53. S. Zhao, M. A. O'Leary, S. Nioka, and B. Chance, "Breast tumor detection using continuous wave light source," in *Optical Tomography, Photon Migration, and Spectroscopy of Tissue and Model Media: Theory, Human Studies, and Instrumentation*, B. Chance and R. R. Alfano, eds., Proc. SPIE **2389,** 809–817 (1995).
54. H. L. Graber, R. Aronson, and R. L. Barbour are preparing a manuscript to be called "Dependence of object sensitivity and resolution on optical thickness of scattering media."